JACS
JOURNAL OF THE AMERICAN CHEMICAL SOCIETY
Article
pubs.acs.org/JACS

Cyclo-P_3 Complexes of Vanadium: Redox Properties and Origin of the ^{31}P NMR Chemical Shift

Balazs Pinter,[†,‡] Kyle T. Smith,[§] Masahiro Kamitani,[§] Eva M. Zolnhofer,[∥] Ba L. Tran,[§] Skye Fortier,[§] Maren Pink,[†] Gang Wu,[⊥] Brian C. Manor,[§] Karsten Meyer,[∥] Mu-Hyun Baik,*[,†,#] and Daniel J. Mindiola*[,§]

[†]Department of Chemistry and the Molecular Structure Center, Indiana University, Bloomington, Indiana 47405, United States
[‡]Eenheid Algemene Chemie (ALGC), Vrije Universiteit Brussel (VUB), Pleinlaan 2, 1050 Brussels, Belgium
[§]Department of Chemistry, University of Pennsylvania, 231 South 34th Street, Philadelphia Pennsylvania 19104, United States
[∥]Department of Chemistry and Pharmacy, Inorganic Chemistry, Friedrich Alexander University Erlangen-Nürnberg (FAU), Egerlandstr. 1, 91058 Erlangen, Germany
[⊥]Department of Chemistry, Queen's University, Kingston, Ontario, Canada K7L 3N6
[#]Department of Chemistry, Korea Advanced Institute of Science and Technology, 34141 Daejeon, Korea

Supporting Information

ABSTRACT: The synthesis and characterization of two high-valent vanadium–*cyclo*-P_3 complexes, (nacnac)V(*cyclo*-P_3)(Ntolyl$_2$) (**1**) and (nacnac)V(*cyclo*-P_3)(OAr) (**2**), and an inverted sandwich derivative, [(nacnac)V(Ntolyl$_2$)]$_2$(μ_2-η^3:η^2-*cyclo*-P_3) (**3**), are presented. These novel complexes are prepared by activating white phosphorus (P_4) with three-coordinate vanadium(II) precursors. Structural metrics, redox behavior, and DFT electronic structure analysis indicate that a [*cyclo*-P_3]$^{3-}$ ligand is bound to a V(V) center in monomeric species **1** and **2**. A salient feature of these new *cyclo*-P_3 complexes is their significantly downfield shifted (by ∼300 ppm) ^{31}P NMR resonances, which is highly unusual compared to related complexes such as (Ar[^{i}Pr]N)$_3$Mo(*cyclo*-P_3) (**4**) and other *cyclo*-P_3 complexes that display significantly upfield shifted resonances. This NMR spectroscopic signature was thus far thought to be a diagnostic property for the *cyclo*-P_3 ligand related to its acute endocyclic angle. Using DFT calculations, we scrutinized and conceptualized the origin of the unusual chemical shifts seen in this new class of complexes. Our analysis provides an intuitive rational paradigm for understanding the experimental ^{31}P NMR spectroscopic signature by relating the nuclear magnetic shielding with the electronic structure of the molecule, especially with the characteristics of metal–*cyclo*-P_3 bonding.

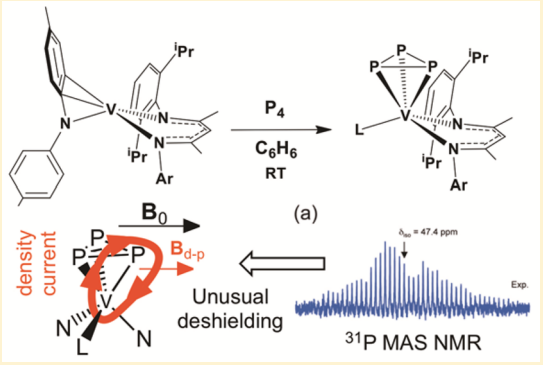

INTRODUCTION

Utilizing white P_4 for the construction of organophosphorus reagents is a practical method for commercially incorporating phosphorus into value-added chemicals.[1,2] White P_4 can also be used for delivering phosphorus atoms to transition metals.[1] In particular, metal complexes in which a *cyclo*-P_3 fragment acts as a formally trianionic ligand with the metal center occupying the fourth vertex of tetrahedron have attracted much attention.[1−6] These *cyclo*-P_3 ligands are unusual and inspiring not only because of their origin of formation[3−5] but also because of their unique bonding and spectroscopic features. Other examples include binuclear inverted sandwich complexes with the *cyclo*-P_3 ligand in a (μ_2:η^3,η^3) bridging mode.[7−18] The body of this work was recently reviewed elsewhere.[1,12]

We became interested in *cyclo*-P_3 complexes because they are proposed to form via a metal-phosphide intermediate that adds to free P_2.[3−5] Specifically, recent studies speculated that metal–*cyclo*-P_3 complexes derive from two possible pathways: one involving P_2 addition to a monometallic phosphide and the second invoking P removal during a bimolecular reaction of a metal–P_4 intermediate.[3] Irrespective of which mechanism is operative, a terminal phosphide could exist en route to the final metal–*cyclo*-P_3 complex. Most of the known *cyclo*-P_3 complexes include late metals,[7−17] whereas, in contrast, early transition metal analogues are scarce,[3−6,18−22] probably due to the rarity of low-valent metal fragments capable of reducing the P_4 unit by multiple electrons and the mismatch in orbital energies between the soft phosphorus and these hard transition metal ions.[1] Only recently have high-valent examples of anionic L$_3$Nb(V) *cyclo*-P_3 complexes (L$^-$ = N[CH$_2$^{t}Bu](3,5-Me$_2$C$_6$H$_3$), O{2,6-^{i}Pr$_2$C$_6$H$_3$})[4−6,18] and a neutral vanadium(V) complex (nacnac)V(*cyclo*-P_3)(Ntolyl$_2$) (**1**) (nacnac$^-$ = [ArNCCH$_3$]$_2$CH, tolyl = 4-MeC$_6$H$_4$)[21] been reported. Notably, some of these complexes have been shown to readily deliver the [*cyclo*-P_3]$^{3-}$ unit to various main group electrophiles and form

Received: September 24, 2015
Published: November 6, 2015

DOI: 10.1021/jacs.5b10074
J. Am. Chem. Soc. 2015, 137, 15247−15261

new tetrahedron allotropes with different pnictogenic elements, such as P and As.[6,18,23]

In this work, we report the synthesis, full characterization, and reactivity studies of two neutral vanadium complexes carrying the $[cyclo\text{-}P_3]^{3-}$ ligand, namely, (nacnac)V(*cyclo*-P_3)(Ntolyl$_2$) (**1**),[19] its closely related derivative (nacnac)V(*cyclo*-P_3)(OAr) (**2**) ($^-$OAr = O{2,6-^{i}Pr$_2$C$_6$H$_3$}), a symmetrical μ_2:η^3,η^3-*cyclo*-P_3 complex connecting two vanadium centers (**3**), and a rare example of a radical anion of **1**. Vanadium can easily access various oxidation states, therefore also allowing us to explore the redox capabilities of the V(*cyclo*-P_3) scaffold at different redox states. In this context, it is worth mentioning that the pioneering work of Fabbrizzi and Sacconi revealed a three-electron redox series for the M(*cyclo*-P_3)M core (M = Co and Ni) displaying a total of 30−33 valence electrons.[24] In addition, the ^{31}P NMR spectroscopic features are particularly interesting, and a combination of solid-state structural studies, solution and solid-state ^{31}P NMR spectroscopic techniques, and theoretical methods have been used to understand them. To date, there is no detailed understanding of the chemical shifts for this special class of P_3-containing molecules, and the origin of their ^{31}P NMR spectroscopic chemical shifts has not been properly addressed in the literature.

RESULTS AND DISCUSSION

Synthesis of Vanadium(V) *Cyclo*-P_3 Complexes. Addition of a slight excess of white P_4 to a deep red solution containing the masked three-coordinate vanadium(II) complex (nacnac)V(Ntolyl$_2$)[19] results in an immediate color change to yellow-brown, forming **1** in 68% yield (Scheme 1). Complex **1**

Scheme 1. Several Routes To Prepare Compounds 1 and 2 by White P_4 Activation

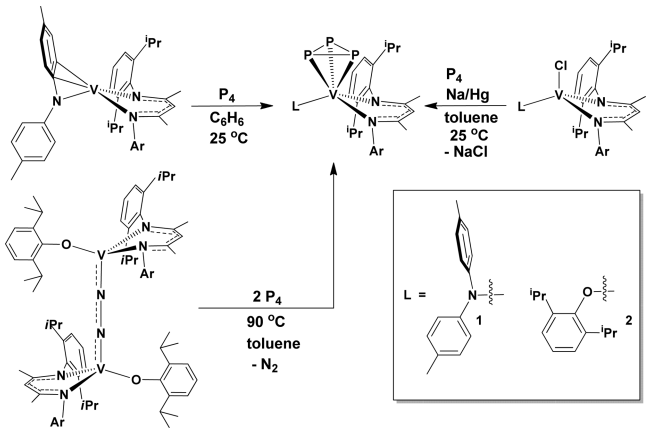

has been previously reported[19] and can also be prepared in 40% yield via Na/Hg reduction (1.5 equiv, 0.5% Na) of (nacnac)VCl(Ntolyl$_2$) in benzene and in the presence of white P_4 (Scheme 1). Cummins and co-workers applied a similar strategy using Rothwell's complex NbCl$_2$(OAr)$_3$[25] ($^-$OAr = O{2,6-^{i}Pr$_2$C$_6$H$_3$}) and excess Na/Hg in THF with white P_4 to form the *cyclo*-P_3 salt $[Na(THF)_3][(ArO)_3Nb(cyclo\text{-}P_3)]$.[6,18] Analogously, complex **2** can be prepared by treating the vanadium(III) precursor (nacnac)VCl(OAr)[26] with Na/Hg in toluene in the presence of white P_4 (Scheme 1). In addition to the simpler multigram-scale preparation of the (nacnac)VCl(OAr) precursor, the isolation of complex **2** is less tedious given its crystallinity when compared to the workup required for complex **1**. An alternative route to complex **2** is to thermalize the dinitrogen complex $[(nacnac)V(OAr)]_2(\mu_2\text{-}\eta^1\text{:}\eta^1\text{-}N_2)$[26] at 90 °C with 2 equiv of P_4 in toluene (Scheme 1). Both yellow-brown-colored complexes are thermally stable up to +100 °C without a noticeable sign of decomposition, and combustion analysis is in agreement with the proposed formulations. Complexes **1** and **2** represent the first examples of *cyclo*-P_3 species of vanadium, which also differ from its heavier congener, $[Na(THF)_x][(ArO)_3Nb(cyclo\text{-}P_3)]$,[18] by being neutral and lacking 3-fold symmetry.

The stoichiometry of P_4 is critically important for the formation of compounds **1** and **2**. When a depleted amount of P_4 (0.25 equiv) is treated with (nacnac)V(Ntolyl$_2$), we observed the production of a bridging *cyclo*-P_3 complex, $[(nacnac)V(Ntolyl_2)]_2(\mu_2\text{-}\eta^2\text{:}\eta^3\text{-}cyclo\text{-}P_3)$ (**3**), most likely arising from the coupling of **1** with unreacted (nacnac)V(Ntolyl$_2$) (Scheme 2). Indeed, treating freshly prepared **1** with an

Scheme 2. Synthesis of the Bridging *Cyclo*-P_3 Vanadium Complex from the Masked Three-Coordinate Complex (nacnac)V(Ntolyl$_2$)

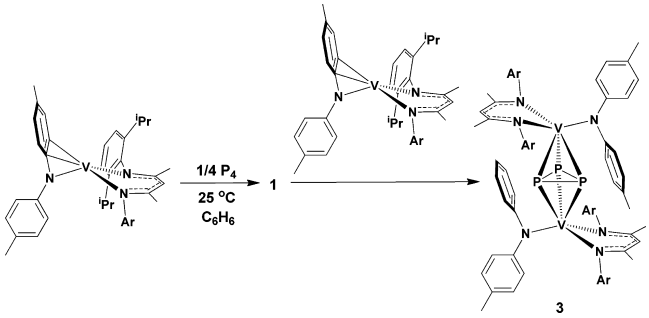

equivalent of (nacnac)V(Ntolyl$_2$) results in a cleaner formation of **3** in quantitative yield without contamination by **1**. Although examples of $\mu_2\text{-}\eta^3\text{:}\eta^3$-*cyclo*-$P_3$ complexes have been reported for late transition metals such as Ni, Co, Pd, and Pt,[1,8,9,12−17] related examples with early transition metals are unknown and rare in the case of electropositive Th(IV) and U(IV).[1,11]

Complex **3** is paramagnetic, and solution-state magnetic data by the method of Evans allowed for the assignment of an overall low-spin $S = {}^1/_2$ spin state at room temperature. Consistent with this, the CW X-band EPR spectrum of **3** in 0.1 mM toluene solution at room temperature features an anisotropic signal centered at $g \approx 2$, whereas no low-field signals were detected. The ^{51}V ($I = {}^7/_2$, 99.75%) hyperfine coupling pattern is rather complicated (Figure 1). If the unpaired electron was coupled only to one ^{51}V nucleus, then a simple eight-line pattern of the EPR signal would result (Robin−Day class I mixed-valence system). If it was completely delocalized over both ^{51}V nuclei, then the signal would be split into 16 lines (Robin−Day class III mixed-valence system). However, in our case, the EPR spectrum of **3** does not show either of these cases, but, instead, it resolves into a 14-line pattern. Thus, the electronic situation in **3** cannot be described by either of the two extreme situations, pointing to this species being a mixed-valence system of Robin−Day class II.[27] At 85 K, a more complicated anisotropic signal is observed (Figure 1).

Structural Studies of Complexes 1−3. We have recently reported the solid-state structure of complex **1**,[19] and the observed metrical parameters of the *cyclo*-P_3 scaffold compare well with the molecular structure of **2** (Figure 2 and Table 1).

DOI: 10.1021/jacs.5b10074
J. Am. Chem. Soc. 2015, 137, 15247−15261

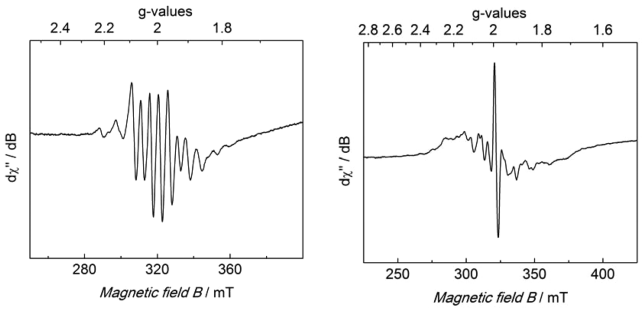

Figure 1. CW X-band EPR spectrum of **3** at room temperature (left) and at 85 K (right), recorded in 0.9 mM THF solution. Experimental conditions: microwave frequency ν = 8.9 GHz, modulation amplitude = 0.3 mT, microwave power = 5 mW, and modulation frequency = 100 kHz.

In both systems, the P−P distances are similar and rather invariant at 2.12−2.14 Å, whereas the V−P distances also remain relatively constant at 2.42−2.44 Å. The P−P distances in *cyclo*-P_3 are slightly shorter than the P−P distance observed in white P_4 (2.18−2.21 Å),[23,28] whereas the P−P distances are somewhat shorter than in the salt $[Na(THF)_3][(cyclo\text{-}P_3)Nb(OAr)_3]$[6,18] or $[Na(THF)]_2[(cyclo\text{-}P_3)Nb(N[Np]Ar)_3]_2$ (Np = $CH_2{}^tBu$)[5] (Table 1). Overall, the metrical parameters are consistent with a symmetrical *cyclo*-$P_3{}^{3-}$ ligand, where the vanadium center occupies the forth site of a metallophosphorotetrahedron. To accommodate the $[cyclo\text{-}P_3]^{3-}$ ligand in complexes **1** and **2**, the nacnac ligand pushes the metal ion above the NCCCN ring plane by 0.89 Å and 43.4°. The flanking NAr groups of nacnac orient themselves with the ^{i}Pr groups pushing away from the P_3 framework to form a bowl-type environment. The $Ntolyl_2$ or OAr ligands block the P_3 framework by angling themselves with the tolyl or ^{i}Pr groups up and down with respect to the *cyclo*-P_3 plane. Table 1 lists metrical parameters of the $P_3{}^{3-}$ ligand in group 5 complexes.

In complex **3**, the structural diagram reveals an inverted sandwich system where the *cyclo*-P_3 scaffold bridges two $(nacnac)V(Ntolyl_2)$ fragments. Each vanadium center is best regarded as tetrahedral (Figure 2). Overall and apart from the slightly more activated P−P distance in the *cyclo*-P_3 unit, there is no significant structural change at each vanadium center when compared to that of monomer **1** except that one vanadium center interacts less with the *cyclo*-P_3 unit than the other when judged by the V−P distances (Figure 2). Hence, while one vanadium center clearly engages the P_3 unit in an η^3-P_3 fashion (V−P distances are 2.4722(8), 2.5001(8), and 2.5022(8) Å), the other one is in accord with an η^2 coordination mode with a notably elongated V−P bond (V1−P1 = 2.9288(9) Å), conforming with the complex EPR signals discussed above. This μ_2-η^2:η^3-*cyclo*-P_3 binding mode is quite unique and, to our knowledge, has been observed only for a very limited number of d^8 metals, $[(triphos)Ni(cyclo\text{-}P_3)Pt(PH_3)_2]^{+1}$, and $[Au\{M(tppme)(cyclo\text{-}P_3)\}_2]^+$ (M = Co, Rh, and Ir).[29,30] Irrespective of this finding, it is very likely that the system is fluxional at room temperature, yielding an overall averaged μ_2-η^3:η^3-*cyclo*-P_3 interaction since we did not observe inequivalent vanadium centers by ^{1}H NMR spectroscopy. The most salient metrical parameters for complex **3** are listed with Figure 2. Compound **3** represents the first example of a group 5 *cyclo*-P_3 bridging two metal centers.[12−17]

Redox Properties of Complexes 1 and 2 and Theoretical Studies of the *Cyclo*-P_3 Ligand. Given the potentially redox-active nature of the *cyclo*-P_3 as well as the vanadium(V) center, we explored the redox properties of complexes **1** and **2** electrochemically and chemically. Cyclic voltammetry studies of **1** revealed an irreversible anodic wave at ~0.7 V vs $FeCp_2{}^{0/+}$ at 0.0 V, whereas a reversible cathodic wave was observed at −1.5 V. The reversibility of this one- electron-reduction process was confirmed unequivocally by linear correlation of the current versus the square root of the scan rate (Figure 3, left). However, the peak-to-peak separation for this Coulombic response of 330 mV indicates some degree of structural rearrangement[31−33] in the complex upon addition of an electron. The time scale of this structural rearrangement is longer than that of the outer sphere electron transfer since it is manifested in a larger than ideal peak-to-peak separation in the cyclic voltammogram, which was, indeed, observed experimentally. In the case of complex **2**, electrochemical reduction also reveals an irreversible anodic wave, whereas the recorded cathodic wave shows a reversible one-electron process at

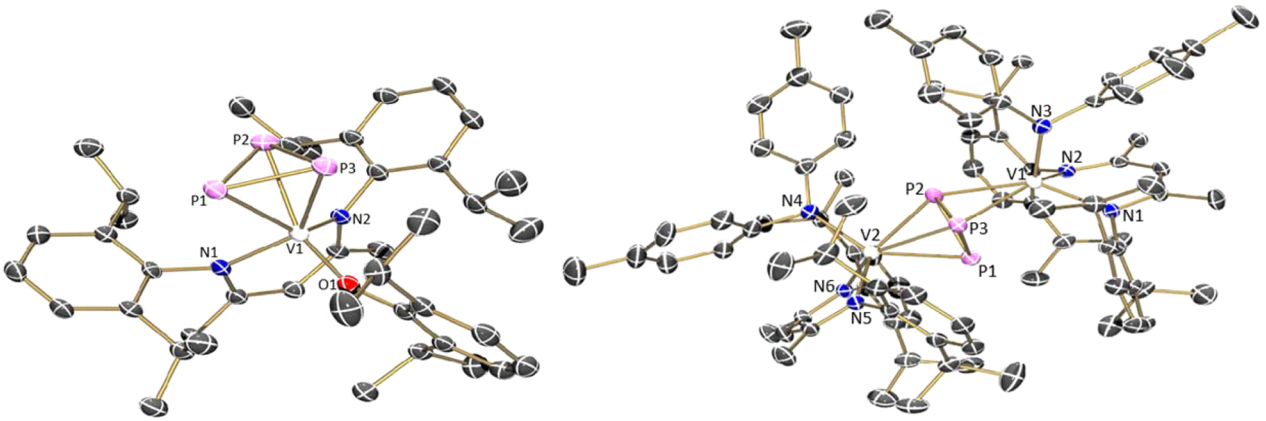

Figure 2. Structural diagrams (50% probability level) of complexes **2** (left) and **3** (right). Disordered solvent and H atoms and ^{i}Pr on the aryl groups on the β-diketiminate have been omitted for clarity. Salient metrical parameters for **2** are listed in Table 1. Distances in Å and angles in degrees for **3**: V1−N3, 1.937(2); V1−N1, 2.089(2); V1−N2, 2.091(2); V1−P2, 2.5279(8); V1−P3, 2.5381(8); V1−P1, 2.9288(9); V2−N6, 1.953(2); V2−N5, 2.043(2); V2−N4, 2.051(2); V2−P2, 2.4722(8); V2−P3, 2.5001(8); V2−P1, 2.5022(8); P1−P2, 2.1804(9); P1−P3, 2.2155(9); P2−P3, 2.1658(10); N3−V1−N1, 100.92(8); N3−V1−N2, 102.44(8); N1−V1−N2, 88.85(8); N6−V2−N5, 106.00(9); N6−V2−N4, 104.62(9); N5−V2−N4, 89.51(8); P2−P1−P3, 59.03(3); P3−P2−P1, 61.29(3); P2−P3−P1, 59.68(3).

DOI: 10.1021/jacs.5b10074
J. Am. Chem. Soc. 2015, 137, 15247−15261

Table 1. Selected Metrical Parameters (Distances in Å and Angles in Degrees) for High-Valent Group 5 *Cyclo*-P_3 Complexes[a]

	1	2[a]	$[1]^{\bullet-}$[b]	$[Na(THF)_3]$ [(*cyclo*-P_3)Nb$(OAr)_3$]	$[Na(THF)]_2[$(*cyclo*-P_3)Nb$(N[Np]Ar)_3]_2$
M–P1	2.4300(9)	2.4236(11)	2.423(9)	2.5122(18)	2.5447(5)
M–P2	2.4388(9)	2.4210(11)	2.439(9)	2.525(2)	2.5272(5)
M–P3	2.4328(9)	2.4719(12)	2.445(9)	2.515(2)	2.5456(5)
P1–P2	2.124(1)	2.1533(14)	2.143(2)	2.194(5)	2.1749(7)
P2–P3	2.137(1)	2.1474(15)	2.154(2)	2.205(4)	2.1745(7)
P3–P1	2.137(1)	2.1489(15)	2.171(2)	2.190(4)	2.1724(7)
P1–P2–P3	59.61(4)	59.96(5)	60.71(3)	60.37(11)	59.93(2)
P2–P3–P1	60.21(4)	60.16(5)	59.40(3)	59.90(12)	60.03(2)
P3–P1–P2	60.19(4)	59.89(5)	59.90(3)	59.73(12)	60.04(2)

[a]Compound **2** co-crystallizes with a small fraction of precursor (nacnac)VCl(OAr). [b]Two chemically equivalent but crystallographically independent molecules are confined in the asymmetric unit, and metrical parameters reported here are for one of these molecules.

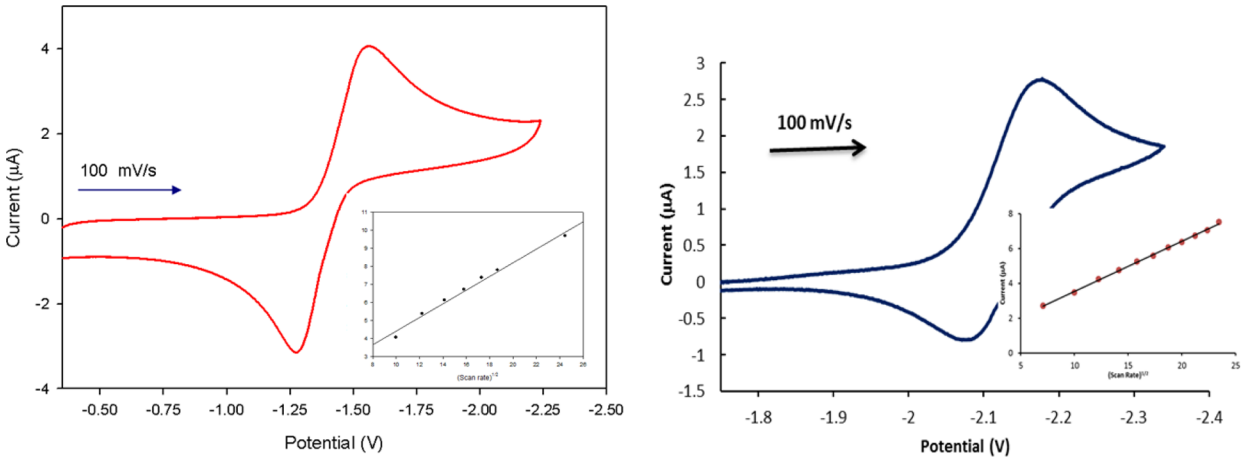

Figure 3. (Left) Cyclic voltammogram of **1** recorded at 100 mV/s in 0.30 M solution of $[N^nBu_4][PF_6]$ in THF at 25 °C with the inset showing reversibility of the one-electron cathodic process, as shown by the scan rate dependence plot. (Right) An analogous cyclic voltammogram of **2** along with the scan rate dependence plot (inset).

around −2.1 V. Akin to **1**, the reduction process is reversible based on the linear correlation between the current and the square root of the scan rate, but, again, the deviation of the peak-to-peak separation (~110 mV) from the ideal Nernstian value of 0.059 V suggests some structural distortions upon addition of an electron to the V(*cyclo*-P_3)(OAr) core (Figure 3, right).

To understand the electronic structures of **1** and **2** and their redox properties, we relied on DFT calculations using the B3LYP[34,35] functional in combination with the cc-pVTZ(-f)[36]/LACV3P basis set, where compound **1** served as a model system. In good agreement with experiments, our calculations predict a reduction potential of −1.502 V vs $FeCp_2^{0/+}$ using the slightly truncated model (nacnac′)V(NPh_2)(*cyclo*-P_3) (**1′**) (nacnac′$^-$ = $[(Ar)NCCH_3]_2CH$, Ph = C_6H_5, Ar = 2,6-$Me_2C_6H_3$). We also found that the computed equilibrium structure of **1′** is very similar to the experimentally determined molecular structure established by single-crystal X-ray diffraction studies. These two benchmarks suggest that the slight structural simplification is admissible and that our computer models capture the most salient features of this molecular system reasonably well. In particular, the excellent agreement between the computed and experimentally observed reduction potentials supports the notion that the electronic structure variations that accompany the redox state changes are captured in at least a plausible fashion. Thus, a more detailed analysis of the bonding is justified and promises to reveal relevant details about how the differential electron density is distributed among the molecular fragments.

A conceptual MO diagram that highlights the most relevant molecular orbitals of the metal–*cyclo*-P_3 interaction is shown in Figure 4. The simplest way to understand the electronic structure of **1** is to construct the key MOs from chemically meaningful molecular fragments. The most plausible building blocks are the $[$(nacnac)V$(Ntolyl_2)]^{3+}$ and $[$*cyclo*-$P_3]^{3-}$ fragments, as shown on the right-hand side of Figure 4. For comparison, we also show the most important molecular orbitals for the 3-fold-symmetric system (*cyclo*-P_3)Mo$(N[^iPr]$-$Ar')_3$ (Ar′ = 3,5-$Me_2C_6H_3$) (**4**) on the left side of Figure 4. Interestingly, the cone angles of trigonal-pyramidal fragments are dramatically different, with V(V) displaying a much more acute cone angle than Mo(VI), as indicated qualitatively in Figure 4. This feature is easy to understand and is a textbook example for second-order Jahn–Teller distortion.[37] As the 3d orbitals of the V(V) center are higher in energy than the 4d orbitals of the Mo(VI) center due to the higher nuclear charge of the latter, the M–L bonding orbitals (not shown in Figure 4) of $[V^VL_3]^{3+}$ will experience a much higher level of second-order mixing, which in turn leads to a more acute angle. This structural distortion is reminiscent of the classical valence angle trends in H_2O, H_2S, and H_2Se.[37]

In Figure 4, differences in energies among the MOs are not drawn to scale but are indicated in a qualitatively consistent fashion. The d^0 configuration in both the $[Mo^{VI}(N[^iPr]Ar')_3]^{3+}$ (**4**) and $[$(nacnac)$V^V(Ntolyl_2)]^{3+}$ (**1**) fragments predicts that all

DOI: 10.1021/jacs.5b10074
J. Am. Chem. Soc. 2015, 137, 15247–15261

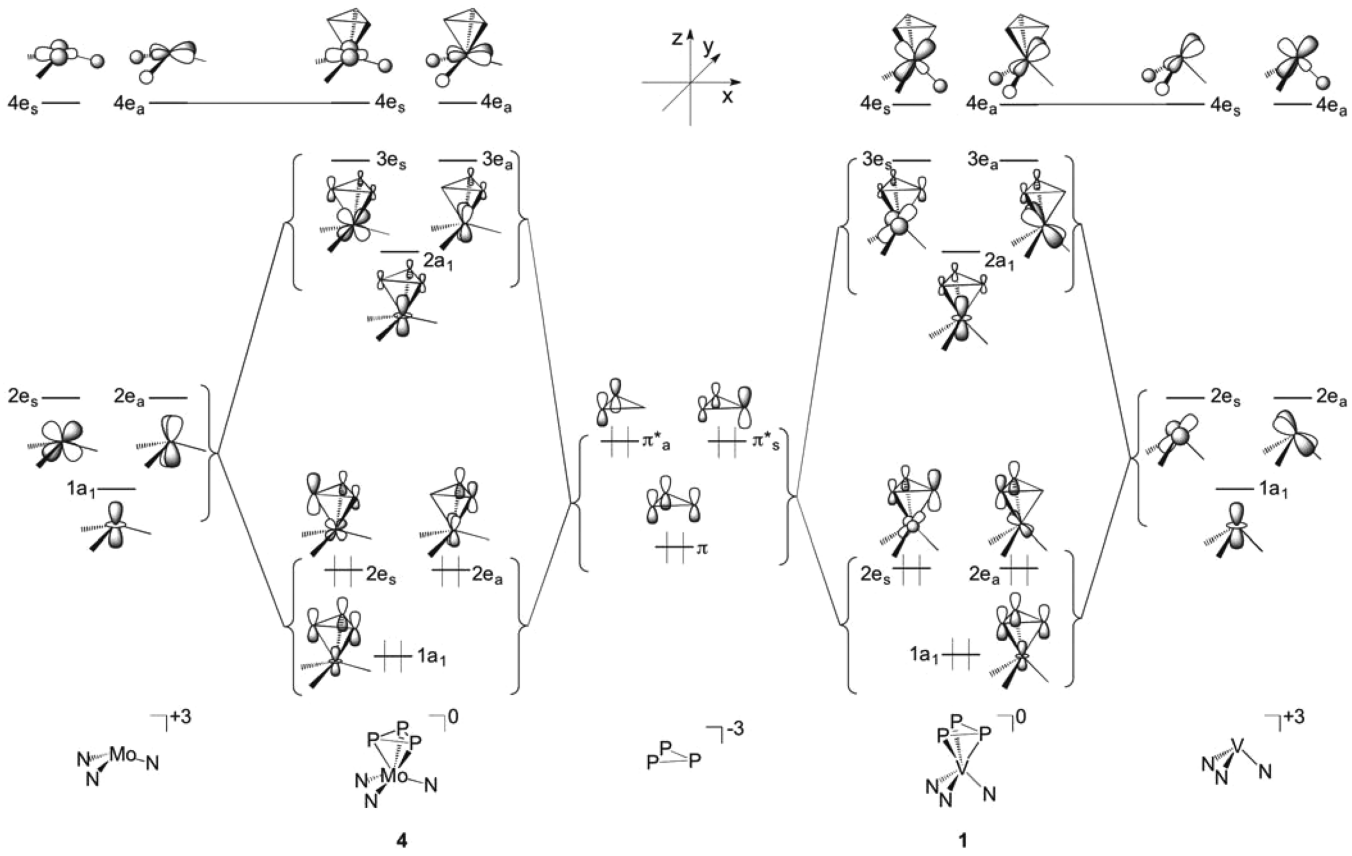

Figure 4. Molecular orbital diagram for the formation of (Ar[^{i}Pr]N)$_3$Mo(*cyclo*-P$_3$) (**4**) and (nacnac)V(*cyclo*-P$_3$)(Ntolyl$_2$) (**1**) from ML$_3^{+3}$ and *cyclo*-P$_3^{3-}$ fragments. Note the effect of pyramidalization on the characteristics of 2e fragment orbitals resulting in different preferred geometries: staggered for molybdenum complex **4** (left) and eclipsed for vanadium species **1** (right).

five metal-dominated frontier orbitals should be empty. Indeed, the three low-lying nonbonding frontier MOs of the ML$_3^{3+}$ fragments, of which the 1a$_1$ orbital contains mostly the metal d$_{z2}$ orbital whereas the 2e$_a$ and 2e$_s$ orbitals are stringly d−π in character, are empty. We use the subscripts 'a' and 's' to denote that the individual orbital is antisymmetric or symmetric with respect to the 2σ transformation, respectively. The remaining two d orbitals with M−L antibonding character form the much higher-lying e set, 4e$_s$ and 4e$_a$. Considerable M−*cyclo*-P$_3$ interactions evolve when the three filled π orbitals of the *cyclo*-P$_3^{3-}$ fragment combine with three low-lying d orbitals: a σ-type interaction is formed when P$_3$−π_1 MO donates electrons to the d$_{z2}$-based 1a$_1$ orbital, whereas the degenerate π^*_a and π^*_s orbitals interact with the 2e set to form two π type interactions. Note that the composition of the 2e MOs depends on the cone angle of the ML$_3^{3+}$ fragment. As the MoL$_3^{3+}$ moiety mostly maintains a wide cone angle, the P$_3$ fragment is bound in a staggered orientation, whereas VL$_3^{3+}$ with a more acute cone angle prefers an eclipsed arrangement.

The MO diagram shown in Figure 4 predicts that the reduction of **1** should result in the population of the antibonding 2a$_1$, 3e$_s$, and 3e$_a$ orbitals. Since these orbitals are σ and π antibonding with respect to the V−P$_3$ interaction in **1**, adding electrons to these orbitals should weaken the V−P$_3$ interaction. Reduction of the V metal should make it a less potent π-acid in general and, thus, weaken the π-bonding interactions with the ancillary ligands nacnac and NPh$_2$ as well. As a result, V−N$_{nacnac}$ distances and the V−NPh$_2$ distances should elongate upon reduction of **1**, which is what is seen in our calculations and solid-state structural data (vide infra).

Chemical reduction of **1** with an outer sphere reductant such as CoCp*$_2$ (reduction potential of −1.91 V in MeCN)[38] results in clean formation of the radical anion salt [CoCp*$_2$][**1**] in

Scheme 3. Synthesis of the Radical Anion of 1 Using CoCp*$_2$

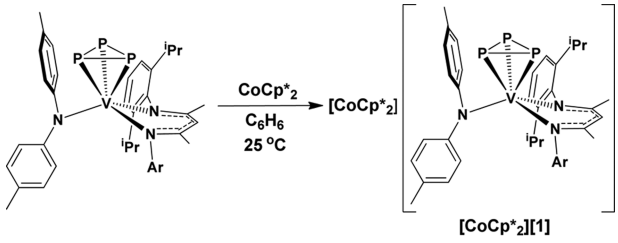

63% yield as an blue-green colored material (Scheme 3). The ^{1}H NMR spectrum of [CoCp*$_2$][**1**] suggests the formation a paramagnetic species, and the solution-state magnetic measurement by the method of Evans reveals μ_{eff} = 1.87μ_B, consistent with a monoradical species. CW X-band EPR measurements of [CoCp*$_2$][**1**] in 0.1 mM THF solution at room temperature clearly demonstrate the $S = {}^1/_2$ nature of the complex, which is in agreement with a vanadium center in a +IV oxidation state. The observed EPR spectrum features an isotropic signal centered at g_{iso} = 1.973 with the typical eight-line splitting pattern, which is due to hyperfine coupling of the unpaired electron to one ^{51}V ($I = {}^7/_2$, 99.75%) nucleus (Figure 5). The

DOI: 10.1021/jacs.5b10074
J. Am. Chem. Soc. 2015, 137, 15247−15261

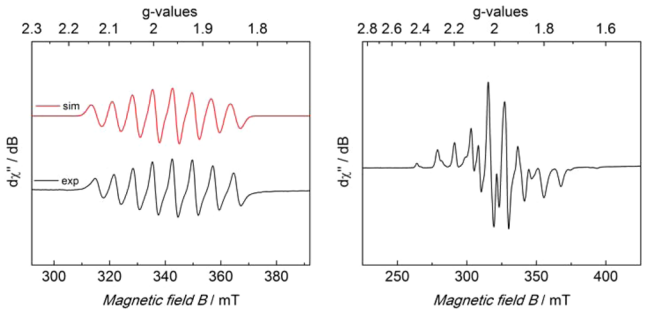

Figure 5. (Left) CW X-band EPR spectrum of $[CoCp^*_2][\mathbf{1}]$ at room temperature recorded in 0.1 mM THF solution (black trace) and its simulation (red trace). Experimental conditions: microwave frequency ν = 9.4 GHz, modulation amplitude = 0.4 mT, microwave power = 10 mW, and modulation frequency = 100 kHz. Simulation parameters: effective spin S = $^1/_2$, g_{iso} = 1.973, line width W_{iso} = 1.45 mT, hyperfine coupling $A_{iso(V)}$ = 196 MHz (7.11 mT), quadratic A-strain C_{2iso} = 4.89 MHz, and linear A-strain E_{iso} = 0.000915 MHz. (Right) CW X-band EPR spectrum of $[CoCp^*_2][\mathbf{1}]$ at 85 K recorded in 0.3 mM THF solution (black trace). Experimental conditions: microwave frequency ν = 9.0 GHz, modulation amplitude = 0.3 mT, microwave power = 1 mW, and modulation frequency = 100 kHz.

signal was simulated with an effective g-value g_{iso} = 1.973, line width W_{iso} = 1.45 mT, hyperfine coupling $A_{iso(V)}$ = 196 MHz (7.11 mT), quadratic A-strain C_{2iso} = 4.89, and linear A-strain E_{iso} = 0.000915. At 85 K, a more complicated anisotropic signal at $g \approx 2$ with an eight-line hyperfine splitting pattern is observed.

In order to probe the degree of structural change in the radical anion component, $\mathbf{1}^{\bullet-}$, as a result of reduction, we collected X-ray diffraction data on a single crystal of $[CoCp^*_2][\mathbf{1}]$ grown from a concentrated THF solution at −37 °C. Figure 6 depicts the solid-state structure of

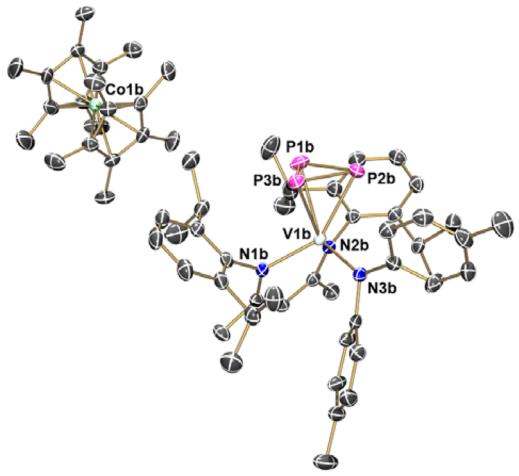

Figure 6. Structural diagram (50% probability level) of compound $[CoCp^*_2][\mathbf{1}]$. H atoms, solvent (Et_2O and toluene), and a crystallographically independent molecule of $[CoCp^*_2][\mathbf{1}]$ have been excluded for clarity. Salient metrical data are listed in Table 1.

$[CoCp^*_2][\mathbf{1}]$, clearly revealing a nearly intact *cyclo*-P_3 ligand along with formation of a discrete salt. Although there is a slight increase in the P−P and V−P distances (Table 1), the most notable change is the elongation of the V−N_{nacnac} distances (1.988(2) Å and 2.029(2) Å in **1** to 2.114(4) Å in $[CoCp^*_2][\mathbf{1}]$) and V−Ntolyl$_2$ distances (1.911(2) Å in **1** to 2.101(8) Å in $[CoCp^*_2][\mathbf{1}]$). As noted earlier, this structural distortion was predicted by DFT due to the LUMOs being augmented with V−N_{nacnac} and V−Ntolyl$_2$ π^* character (see Figure 4 for computed MOs).

NMR Spectroscopic Characterization. At room temperature, the ^{1}H NMR spectrum of **1** displays C_s symmetry with locked NAr groups of the nacnac ligand (four diastereotopic ^{i}Pr methyl groups and two ^{i}Pr methine resonances). Cooling a solution of **1** to −60 °C did not generate a static *cyclo*-P_3 ligand, as implied by ^{31}P NMR spectroscopy. This feature is not surprising since DFT calculations suggest the upper limit to be 14.53 kcal mol^{-1} for the rotational barrier of the *cyclo*-P_3 fragment. Complex **2** displays similar C_s symmetry in solution with four diastereotopic ^{i}Pr groups in addition to another ^{i}Pr environment for the OAr.

^{31}P NMR Studies. The chemical shift of an NMR-active nucleus is not only useful for precisely determining the identity of a molecule in solution but also can be used as a diagnostic tool that directly reports on the chemical environment of that nucleus. Most intuitively, the magnetic shielding is directly correlated to the electron density: as the electron density around a nucleus is increased, for example, by an electron-donating functional group in close proximity, the nucleus should experience a higher degree of shielding and, therefore, the resonance frequency should shift upfield. This intuitive and useful relationship is, unfortunately, obeyed strictly only in ^{1}H NMR spectroscopy where the diamagnetic component of the magnetic shielding, σ^d, dominates the overall shielding. Because heavier nuclei, such as ^{13}C and ^{31}P, have access to p and d (theoretically speaking) orbitals that form low-energy molecular orbitals, the electron density around these nuclei is much more dynamic in the sense that local fluctuations of the electron cloud become much more common than are seen for protons. The magnetic shielding that arises from these electron density fluctuations is commonly referred to as paramagnetic shielding, σ^p, and is typically more sensitive to the changes in chemical bonding than the diamagnetic shielding. One manifestation of this relationship is that the chemical shift range observed in ^{1}H NMR spectra is much smaller than in ^{13}C or ^{31}P NMR spectra.

Previously, it was reported that the ^{31}P NMR spectra of *cyclo*-P_3 complexes show a highly upfield-shifted singlet between −170 and −223 ppm. This spectral feature is reminiscent of what was observed in other polyphosphorus compounds with small endocyclic angles.[1,17,12d] Unlike the 3-fold-symmetric *cyclo*-P_3 complexes of W,[20] Mo,[3] and Nb,[4−6] **1** and **2** show a ^{31}P NMR resonance at room temperature that is significantly downfield-shifted to 85.0 ($\Delta\nu_{1/2}$ = 234 Hz) and 125.0 ($\Delta\nu_{1/2}$ = 324 Hz) ppm, respectively. In comparison, complex $[CoCp_2]$-$[(cyclo\text{-}P_3)Nb(OAr)_3]$ was reported to have a ^{31}P NMR signal at −170 ppm; although no structural information was provided,[6] it is probable that this signal originated from a 3-fold-symmetric Nb-(*cyclo*-P_3) entity. Likewise, the derivative $[Na(THF)]_2[(cyclo\text{-}P_3)Nb(N[Np]Ar)_3]_2$,[4,5] which exists as a dimer in solution and in the solid state,[5] shows an even further upfield-shifted resonance at −223 ppm. Both the solid-state structure and low-temperature solution ^{31}P NMR spectra are in accord with loss of the 3-fold symmetry.[5] The discrete salt $[Na(12\text{-crown-}4)_2][(cyclo\text{-}P_3)Nb(N[Np]Ar)_3]$ also shows a highly shielded ^{31}P NMR resonance at −183 ppm.[5] Notably, Wolmershäuser and Scheer's *cyclo*-P_3 complexes $CpMo(CO)_2(cyclo\text{-}P_3)$ and $CpCr(CO)_2(cyclo\text{-}P_3)$ display even more shielded ^{31}P NMR resonance at −352 and −285 ppm,

DOI: 10.1021/jacs.5b10074
J. Am. Chem. Soc. 2015, 137, 15247−15261

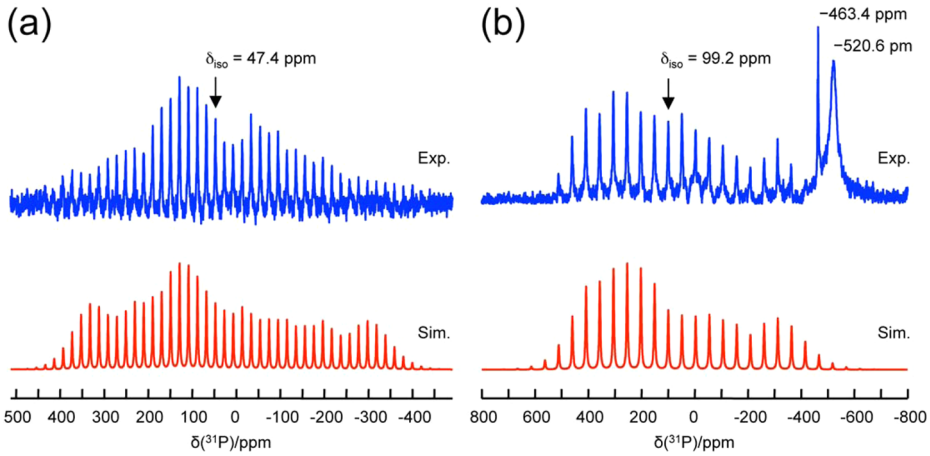

Figure 7. Experimental and simulated ^{31}P MAS NMR spectra for complexes **1** (a) and **2** (b). The sample spinning frequency was 5.0 and 12.5 kHz in (a) and (b), respectively. In (a) the signal intensity distortions at the outer edges of the experimental spectrum are due to insufficient RF excitation. Unfortunately, the solid sample decomposed inside the rotor after this spectrum was collected. In (b), the signals at −463 and −521 ppm are due to the presence of a liquid-like and solid form of P_4, respectively.

respectively,[22a,b] whereas Goh's Cp* derivatives of Mo and W, Cp*Mo(CO)$_2$(*cyclo*-P$_3$) and Cp*W(CO)$_2$(*cyclo*-P$_3$), have been shown to display similar chemical shifts.[21] These resonances are mostly invariant to temperature drifting and change by less than 1 ppm when the solution is cooled.

As mentioned above, the relatively large upfield shifts of the ^{31}P NMR resonances were previously explained as being due to the small endocyclic angles of the P_3 unit. In critically evaluating this rationale, we must admit that, except for empirically recognizing the common element of the acute angle in the *cyclo*-P_3 ligand, there was no real explanation for why an acute endocyclic angle would give rise to the observed upfield shift of the ^{31}P NMR resonances. This frustrating observation serves to illustrate the difficulty in understanding chemical shifts that are dominated by paramagnetic shielding, as mentioned above. Given that **1** and **2** contain a similar, if not identical, *cyclo*-P_3 fragment as that in all other related complexes, which nevertheless display significantly different ^{31}P NMR chemical shifts, this widely accepted paradigm may have to be reconsidered. To obtain more experimental data that may help to explain the origin of the ^{31}P NMR chemical shifts for this class of ligands and to provide a solid foundation for the computational study (vide infra), we obtained the solid-state ^{31}P NMR spectra for **1** (δ_{iso}(^{31}P) = 47 ppm) and **2** (δ_{iso}(^{31}P) = 99 ppm) via magic-angle spinning (MAS) techniques, as shown in Figure 7. In addition to displaying similar isotropic ^{31}P chemical shifts as seen in solution, these solid-state ^{31}P NMR spectra reveal the presence of significant chemical shift anisotropies (CSA); the respective chemical shift tensors can be obtained from analysis of the rotational sidebands, as illustrated in Figure 7. For complex **1**, the principal tensor components, δ_{11} = 400 ppm, δ_{22} = 120 ppm, and δ_{33} = −380 ppm, span a wide range of ∼800 ppm, whereas for **2**, the tensor components are δ_{11} = 522 ppm, δ_{22} = 255 ppm, and δ_{33} = −480 ppm. The results of solution- and solid-state ^{13}P NMR spectroscopy of **1** and **2** are clearly consistent with a downfield chemical shift and suggest critical differences in the electronic environment at phosphorus.

To understand what makes **1** and **2** so special, in particular, why the chemical shift tensor component δ_{11} is so notably deshielded, we computed and analyzed the ^{31}P magnetic shielding tensors of the truncated versions (nacnac′)V(NPh$_2$)-(*cyclo*-P_3) (**1′**). To compare this unusual behavior to what may be regarded to as standard behavior, we also examined the C_3 symmetric complex (Ar[^{i}Pr]N)$_3$Mo(*cyclo*-P_3),[3] again using a slightly simplified model (Ph[Me]N)$_3$Mo(*cyclo*-P_3) (**4′**). As noted above, this complex exhibits a highly shielded resonance at −185 ppm that is comparable to the other diamagnetic transition metal *cyclo*-P_3 examples. The magnetic shielding at a NMR-active nucleus and the resulting chemical shift can be calculated from first principles to a reasonable degree of accuracy.[39] Briefly, the following relationships are most relevant for analyzing and understanding the chemical shift of the phosphorus nuclei of the P_3 ligand:[40]

$$\mathbf{B} = \mathbf{B}_0 - \mathbf{B}_i = \mathbf{B}_0 - \sigma\mathbf{B}_0 = (1 - \sigma)\mathbf{B}_0 \quad (1)$$

$$\sigma = \sigma^d + \sigma^p \quad (2)$$

$$\sigma_{ij}^p = \frac{e^2\mu_0}{8\pi m_e} \sum_n \frac{1}{E_{exc} - E_{ground}} \left[\left\langle \phi_{ground} \middle| \sum_k \hat{L}_{ki} \middle| \phi_{exc} \right\rangle \left\langle \phi_{exc} \middle| \frac{\hat{L}_{kNJ}}{r_{kN}^3} \middle| \phi_{ground} \right\rangle + c.c. \right] \quad (3)$$

The magnetic field that a NMR-active nucleus experiences ($\mathbf{B}$) is the sum of the externally applied field ($\mathbf{B}_0$) and the induced magnetic field ($\mathbf{B}_i$), which might be antiparallel (shielding) or parallel (deshielding) to $\mathbf{B}_0$ (eq 1). Since the induced magnetic field $\mathbf{B}_i$ is proportional to the external field $\mathbf{B}_0$, the overall effect of the magnetic field generated by the electrons can be expressed with a single factor, the magnetic shielding parameter σ (eq 1). The overall magnetic shielding parameter σ contains diamagnetic (σ^d) and paramagnetic (σ^p) contributions (eq 2), as stated above. The paramagnetic shielding contribution will be of particular importance, and as noted above, this contribution to the magnetic shielding is not easy to understand as it involves electron density fluctuations that engage both filled and unfilled molecular orbitals as described in eq 3.[41] In the case of the P_3 unit, the most important electron density fluctuations involve ring currents across the molecule that will be induced by the external magnetic field. The magnitude of the mixing between the

DOI: 10.1021/jacs.5b10074
J. Am. Chem. Soc. 2015, 137, 15247−15261

Table 2. Paramagnetic (σ^p), Diamagnetic (σ^d), Combined (σ), and Average Magnetic Shieldings (σ_{avg}) in Addition to Chemical Shifts (δ_{avg}) for the Phosphorus Nuclei of 1′ and 4′[a]

structure	atom	σ^p	σ^d	σ	σ_{avg}	δ_{avg}
1′	P1	−635.5	974.0	338.9	224.5	76.8 [85.0]
	P2	−781.9	972.9	191.0		
	P3	−829.0	972.7	143.7		
4′	P1	−537.1	965.6	428.5	431.1	−129.9 [−185.0]
	P2	−531.9	965.6	433.7		
	P3	−534.4	965.6	431.2		

[a]Values are reported in ppm. Experimental values are provided in brackets.

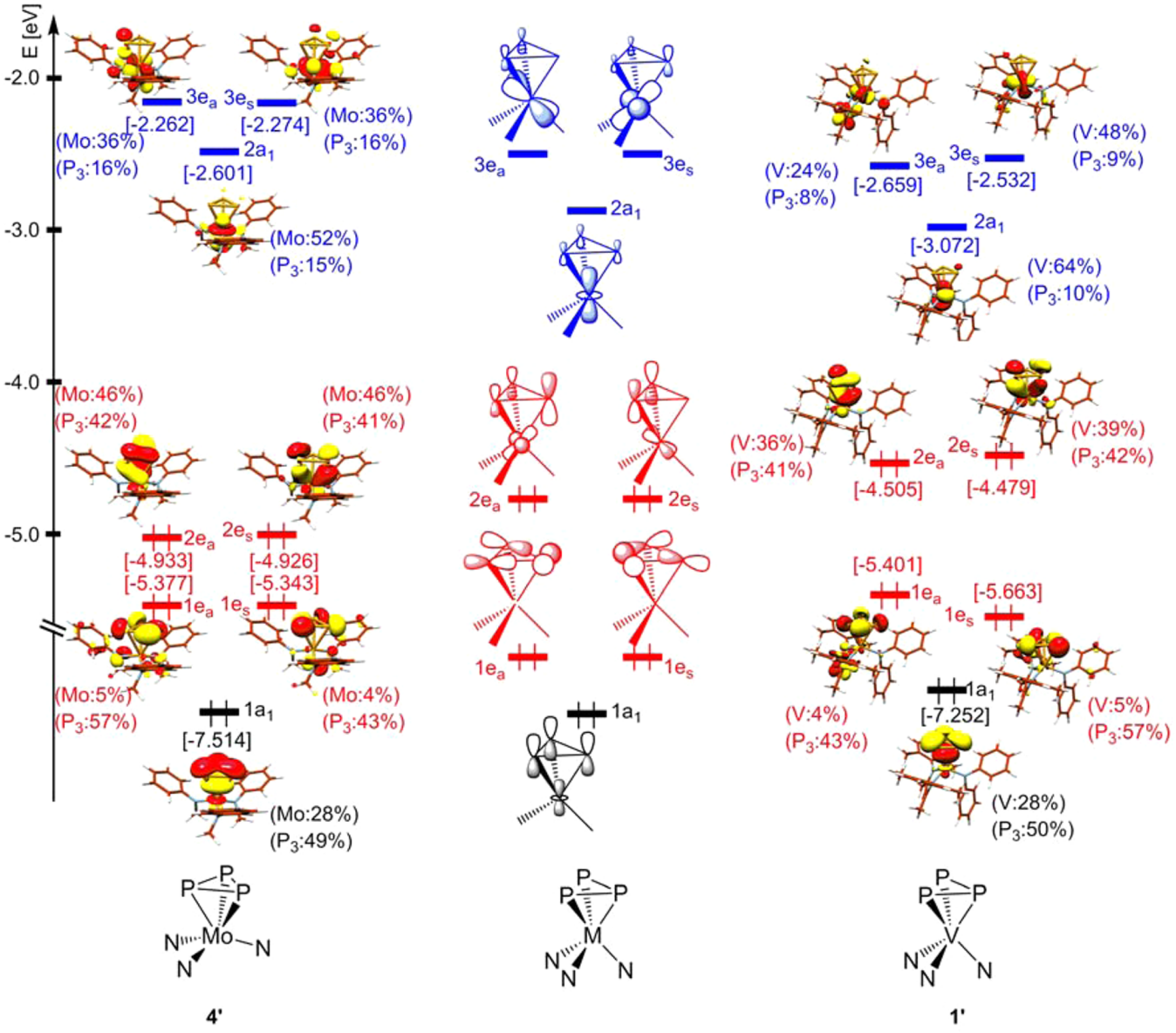

Figure 8. Molecular orbitals that are most responsible for the ^{31}P chemical shift (red and blue) and the most important metal−*cyclo*-P_3 σ-bonding orbital $1a_1$ (black) in 1′ and 4′.

occupied and unoccupied orbitals, which causes these fluctuations, depends on the energy gap between the mixing orbitals ($E_{exc} - E_{ground}$ in eq 3) and on the $\langle|\phi_{exc}|L_k|\phi_{ground}\rangle$ integral, which represents the overlap between mixing orbitals, ϕ_{ground} and ϕ_{exc}, coupling through the angular momentum operator L_k ($k = x, y$, and z).

Table 2 summarizes the calculated diamagnetic and paramagnetic contributions to the shielding for the three phosphorus nuclei in the *cyclo*-P_3 ligand for the models 1′ and 4′. The computed average isotropic chemical shifts of 76.8 ppm for 1′ and −129.9 ppm for 4′ are in reasonable agreement with the measured values of 85.0 and −185 ppm for 1 and (Ar[^{i}Pr]N)$_3$Mo(*cyclo*-P_3), respectively. Most importantly, our

DOI: 10.1021/jacs.5b10074
J. Am. Chem. Soc. 2015, 137, 15247−15261

Table 3. Contributions to the ^{31}P Magnetic Shielding Tensor Components of P_3 Nucleus (in ppm) from Coupling $1e_{s/a}$ and $2e_{s/a}$ Orbitals with Unoccupied $2a_1$ and $3e_{s/a}$ Orbitals in 1′ and 4′[a]

		1’					4’				
Occ. MO	Unocc. MO	ΔE/eV	σ_{iso}	σ_{11}	σ_{22}	σ_{33}	ΔE/eV	σ_{iso}	σ_{11}	σ_{22}	σ_{33}
$1e_s$	$2a_1$	2.591	–	–	–	–	2.776	22.6	24.1	28.4	15.3
	$3e_s$	3.004	-12.1	36.7	-77.1	4.0	3.103	25.7	-3.4	91.2	-10.5
	$3e_a$	3.131	-10.3	-2.9	-27.4	-0.5	3.115	–	–	–	–
$1e_a$	$2a_1$	2.330	–	–	–	–	2.741	-13.4	-41.2	4.2	-3.2
	$3e_s$	2.742	-63.2	**-163.8**	**8.4**	-34.4	3.068	25.9	**72.9**	**-1.4**	6.3
	$3e_a$	2.869	-15.6	-33.2	-3.4	-10.3	3.080	-10.2	-16.6	-0.6	-13.5
$\Sigma 1e \leftrightarrow \Sigma(2a_1+3e)$			**-101.3**					**50.6**			
$2e_s$	$2a_1$	1.433	-188.3	**-564.4**	1.6	-2.2	2.332	-31.9	-4.7	**-87.7**	-3.3
	$3e_s$	1.846	-43.6	8.0	-136.9	-2.0	2.659	-26.9	2.4	-76.3	-6.8
	$3e_a$	1.973	10.5	1.8	29.7	0.0	2.671	-42.5	-96.5	-31.0	-0.1
$2e_a$	$2a_1$	1.407	-15.1	-87.4	8.8	33.3	2.325	23.1	70.2	1.4	-2.2
	$3e_s$	1.820	–	–	–	–	2.652	-45.7	-141.1	0.8	3.2
	$3e_a$	1.947	39.1	1.0	115.9	0.5	2.664	–	–	–	–
$\Sigma 2e \leftrightarrow \Sigma(2a_1+3e)$			**-197.4**					**-124.0**			
$\Sigma(1e+2e) \leftrightarrow \Sigma(2a_1+3e)$			**-298.7**					**-73.4**			

[a]The most important contributions are marked in green and discussed in the main text.

quantum chemical models reproduce the experimentally observed downfield shift of the ^{31}P resonance of 1′ and indicate an upfield shift for 4′. Experimentally, the three phosphorus atoms are considered to be chemically equivalent in 4′, and we expect to see one signal. This is, of course, due to fluxional behavior within the time scale of the conducted NMR spectroscopic experiment. At frozen geometries used in our quantum chemical simulations, the three P nuclei experience very different magnetic fields, as reflected in the predicted ^{31}P resonances that vary by as much as ∼200 ppm in 1′, ranging from 144 to 339 ppm. As explained above, the diamagnetic term depends only on the occupied orbitals and displays a much narrower range of shielding contributions; in 1′, the computed σ^d values are 974.0, 972.9, and 972.7, whereas it is 965.6 ppm for all three phosphorus nuclei in 4′. The paramagnetic contribution, on the other hand, differs significantly for the phosphorus nuclei of 1′, with computed shielding parameters being −635.5, − 781.9, and −829.0 ppm. These values illustrate the general statement made above that σ^p dominates the overall shielding σ_{avg} and, thus, determines the chemical shift δ_{avg} computed against the reference.

Thoroughly analyzing the paramagnetic contribution to the shielding is difficult because it is the sum of a great number of magnetic fields originating from occupied−unoccupied orbital pair couplings through the angular momentum operator. The magnitude of these individual shielding/deshielding terms ranges from, e.g., 200 to −600 ppm in the cases of 1′ and 4′. In addition, the magnetic fields created by what is most intuitively visualized as electron density fluctuations are not easy to envision. As ^{1}H NMR spectroscopy is by far the most widely utilized NMR technique and the chemical shifts encountered here are easy to understand based on the static diamagnetic terms only, the general chemical intuition based on ^{1}H NMR can also be misleading. The key to understanding paramagnetic shielding lies in finding a limited number of specific orbital pairs that make a decisive contribution and that are characteristic for the specific molecule under investigation.[42] In this case, we sought to understand the difference of ∼200 ppm in overall shielding between 1′ and 4′. After an extensive comparison of each individual component that gives rise to the paramagnetic shielding, we identified four occupied orbitals that are mostly responsible for the downfield shift of a few hundred ppm in 1′. These MOs are the in-plane P−P σ-orbitals $1e_s$ and $1e_a$ and the P_3−π orbitals $2e_s$ and $2e_a$, shown in Figure 8 in red. These MOs couple most intensively with the three lowest-lying vacant metal-dominated orbitals $2a_1$, $3e_s$, and $3e_a$ illustrated in Figure 8 in blue. The involvement of these metal-based unoccupied orbitals in paramagnetic shielding is intriguing as it suggests a nontrivial role of the metal for the ligand chemical shift.

Table 3 enumerates the shielding contributions resulting from the coupling of the four occupied orbitals with the three unoccupied MOs that were selected. The total isotropic paramagnetic shielding contribution of these mixings, $\Sigma(1e + 2e) \leftrightarrow \Sigma(2a_1 + 3e)$, is −298.7 ppm for 1′ and −73.4 ppm for 4′. Whereas there are many more contributing orbital mixings to the respective shielding tensors, the couplings between the highest occupied molecular orbitals and the lowest unoccupied orbitals are by far the most important contributors as the energy gap between these MOs is the smallest. Thus, the majority of the difference in chemical shift should be captured by these interactions; indeed, the difference in paramagnetic shielding originating from this subset of MOs accounts for a difference of 225.3 ppm, which is very close to the difference of 206.6 ppm in σ_{avg} when all components were taken into account. This simplification is helpful because the isotropic shielding value can be dissected further beyond the arithmetic mean and the most relevant differences in the shielding tensors

DOI: 10.1021/jacs.5b10074
J. Am. Chem. Soc. 2015, 137, 15247−15261

can be identified. The vectors spanning the principal axis systems (PAS) at each phosphorus atoms are shown in Figure 9

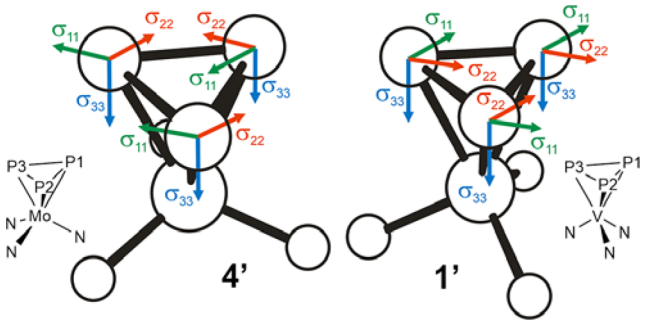

Figure 9. Principal axis systems (PAS) of the ^{31}P magnetic shielding tensors in **1**′ and **4**′.

for **1**′ and **4**′ and denoted σ_{11}, σ_{22}, and σ_{33}; these axes are chosen to force the tensor to have only diagonal elements, i.e., force the off-diagonal elements to vanish. By doing so, the shielding can be decomposed into three principle components that will further simplify the interpretation. Most notably, the shielding is greatest in the σ_{33} direction, which is always perpendicular to the *cyclo*-P_3 plane for all three phosphorus nuclei in both systems, as illustrated in blue in Figure 9. The other two components, σ_{11} and σ_{22}, shown in green and red in Figure 9, respectively, span the *cyclo*-P_3 plane dimension in accord with the PAS convention.[39a] More interestingly, the associated shielding parameters indicate significant deshielding effects along these axes.

Only selected differences of the shielding tensors are highlighted in Table 3 in order to derive intuitive chemical concepts for the M−*cyclo*-P_3 interactions from the ^{31}P NMR spectroscopic chemical shifts. The $2e_s \leftrightarrow 2a_1$ coupling has the largest deshielding contribution of −564.4 ppm (for P_3 nucleus) in the σ_{11} direction for **1**′, whereas the analogous contribution, along the σ_{22} vector in **4**′, is significantly smaller at −87.7 ppm. Note that the principal axis directions between the two molecules are not identical as the molecular structures are different. There are a number of significant differences in how much the other frontier orbitals contribute to the shielding tensors, as enumerated in Table 3. The $(2e_s|2a_1)$ pair interaction, however, is so dominating that it can be considered to be the main reason for the dramatically different chemical shifts of complex **4**′, which displays a chemical shift prototypical for known *cyclo*-P_3 complexes, and complex **1**′, which contains highly deshielded phosphorus nuclei.

As is the case for all orbital−orbital interactions, the coupling efficiency is inversely proportional to the energy difference between the interacting orbitals. Table 3 lists the orbital energy differences: For **1**′, the energy difference between $2e_s$ and $2e_a$, $2a_1$ orbitals is 1.433 eV, whereas a gap of 2.332 eV was computed for **4**′. Thus, the small energy difference between $2e_s$ and $2a_1$ orbitals translates into a very efficient paramagnetic deshielding for **1**′, resulting in a computed additional downfield shift of ∼70 ppm, that is, −197.4 vs −124.0 ppm for **1**′ and **4**′, respectively.

A second significant contributor to creating a different shielding pattern between **1**′ and **4**′ is the coupling of the occupied $1e_a$ orbital with the unoccupied $3e_s$. This mixing results in a significant deshielding of −163.8 ppm in the σ_{11} direction and a negligible shielding of 8.4 ppm in the σ_{22} direction for **1**′. In contrast, in **4**′ the coupling of the same orbitals generates an insignificant magnetic field in the σ_{22} (−1.4 ppm) direction, whereas it induces a strong antiparallel magnetic field with a shielding of 72.9 ppm along the σ_{11} vector. In this case, the energy gaps between the two orbitals are very similar for the two complexes **1**′ and **4**′, namely, 2.742 and 3.068 eV, respectively. Therefore, the rationale that the poor coupling of orbitals is due to orbital energy mismatch cannot account for this difference. In this case, the $\langle 3e_s|L_k|1e_a\rangle$ integrals ($k = \sigma_{11}$ and σ_{22}) are responsible for this behavior. To conceptually understand the sign and magnitude of this integral and to interpret it in chemically meaningful terms, it is useful to recognize how the angular momentum operator L_k acts on an orbital: formally, it initiates a counterclockwise rotation on the orbital along the applied magnetic field.[39a] Its effect is illustrated on the straightforward example of a F_2 molecule in Figure 10a: here, the $\pi_x \leftrightarrow \sigma^*$ coupling makes the largest

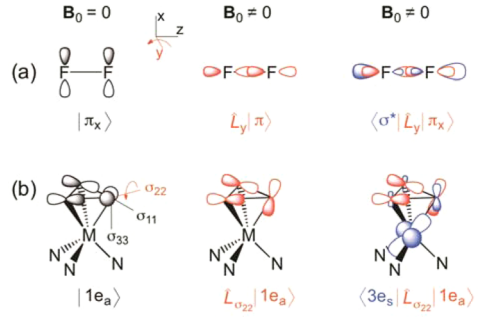

Figure 10. Schematic representation of the operation of L_y on the π_x orbital of F_2 (a) and $L_{\sigma 22}$ on the $1e_a$ orbital of **1**′ (b) and the corresponding mixings of the transformed orbitals with σ^* and $3e_s$, respectively.

contribution to the paramagnetic shielding tensor of the F_2 molecule. The transformed orbital (in red), i.e., $L_y|\pi_x\rangle$, has an extensive overlap with the lowest-lying σ^*, resulting in a large $\langle\sigma^*|L_y|\pi_x\rangle$ integral value. Since the overlap is constructive, i.e., the orbital phases match, the sign of the integral is positive and, accordingly, the resulting magnetic field contributes to the shielding of the F-nuclei.[39a]

Figure 10b shows an approximate but intuitively understandable picture of how the angular momentum operator acts on the $1e_a$ orbital and how it couples with $3e_s$ along the σ_{11} and σ_{22} vectors. Formally, the atomic p orbitals are rotated out of the *cyclo*-P_3 plane pointing into the region between the metal and the *cyclo*-P_3 fragment. Because of the antibonding nature of $3e_s$, the transformed orbital has both constructive and destructive overlaps with the $3e_s$ orbital. The sign of the computed integrals assigns the d−p overlap to be destructive, whereas the overlap of p−p is constructive, as indicated by shading of the orbital lobes in Figure 10b. Accordingly, the $1e_a \leftrightarrow 3e_s$ mixing might lead to both deshielding and shielding of the phosphorus nuclei depending on the relative magnitude of the d−p and p−p overlaps. The calculated $1e_a \leftrightarrow 3e_s$ coupling values, −163.8 for **1**′ and −1.4 ppm for **4**′ along the corresponding axis of σ_{11} and σ_{22}, respectively, indicate that the out-of-phase overlap of the metal atomic d orbital and phosphorus p orbital (d−p) is large for **1**′ but small for **4**′. On the contrary, the positive shielding values of 8.4 and 72.9 ppm computed for **1**′ and **4**′ along the corresponding principal axis, σ_{22} and σ_{11}, respectively, highlight that the p−p overlap is small

DOI: 10.1021/jacs.5b10074
J. Am. Chem. Soc. 2015, 137, 15247−15261

for **1′** but large for **4′**. These shielding values imply that vanadium contributes actively and significantly to the deshielding of P nuclei by means of its unoccupied $3e_s$ orbital in **1′**, whereas it is mostly the *cyclo*-P_3 ligand-based atomic orbitals that affect the shielding in **4′** through $1e_a \leftrightarrow 3e_s$ mixing. Thus, the perhaps unintentionally applied previous rationalization, which considered only the endocyclic angle of the *cyclo*-P_3 ligand and neglected the metal to which the ligand is bound, is at least qualitatively justified for second- and third-row transition metals, where the d orbitals are more compact due to higher effective nuclear charge and relativistic contraction effects.

In summary, we identified two straightforward reasons that will give rise to the observed significant deshielding of phosphorus nuclei in vanadium−(*cyclo*-P_3) complexes in contrast to the otherwise highly shielded and upfield-shifted M−(*cyclo*-P_3) complexes: First, the very small HOMO−LUMO gap of the studied vanadium complexes leads to a very intense coupling of these frontier orbitals ($2e_s \leftrightarrow 2a_1$ coupling) in an external magnetic field. The mixing of $2e_s \leftrightarrow 2a_1$ orbitals generates a magnetic field parallel to $\mathbf{B}_0$ at the phosphorus nuclei, which manifests in strongly downfield-shifted resonances. Second, spatially diffuse, lower-energy, dominantly metal-based unoccupied M−L antibonding orbitals that are most likely encountered in first-row transition metal complexes provide an effective deshielding mechanism by rerouting the electron density fluctuations through the metal center, as explained above using the $1e_a \leftrightarrow 3e_s$ coupling. This latter mechanism of shielding is particularly interesting and has thus far not been recognized as being important. Figure 11 shows a

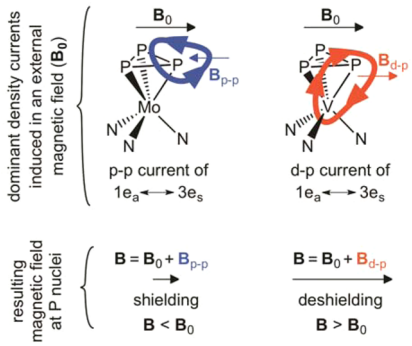

Figure 11. Induced density currents and their shielding/deshielding effect originating from $1e_a \leftrightarrow 3e_s$ mixing.

simplified illustration of how the paramagnetic shielding as a function of induced density currents can be envisioned. Following Ramsey's theory,[40] which forms the basis of eq 3, the paramagnetic shielding is taken as the magnetic effect of the density currents induced by the external magnetic field ($\mathbf{B}_0$). These density currents originate from the mixing of the ground-state wave function of the molecule into low-lying excited states, often approximated by occupied and unoccupied orbitals, respectively. Namely, $\mathbf{B}_0$ induces two major density currents when mixing the $1e_a$ orbital with $3e_s$ along the σ_{11} and σ_{22} principal axes: an intraligand fluctuation emerging from the p−p overlap and a ligand-to-metal current via a d−p overlap. These density currents generate magnetic fields parallel and antiparallel to $\mathbf{B}_0$, respectively. Since the topology of the M−(*cyclo*-P_3) antibonding $3e_s$ orbital is different for **1′** and **4′**, namely, more metal-based for **1′**, the ligand-to-metal current (d−p overlap) becomes dominant in **1′**, which deshields the phosphorus nuclei. In short, both the small HOMO−LUMO gap and the dominant metal contribution to the low-lying antibonding M−(*cyclo*-P_3) orbitals lead to intensive, metal-involved density currents in **1′**, generating magnetic fields parallel to $\mathbf{B}_0$ that manifest in strongly downfield-shifted phosphorus resonances.

CONCLUSIONS

Prior to this work, the formation of monomeric *cyclo*-P_3, or P_4 activation in general, supported by vanadium has never been reported owing to the lack of synthetic access to low-valent and low-coordinate vanadium(II) synthons. We demonstrated with this work that reactive three-coordinate vanadium(II) platforms can be utilized to perform three-electron chemistry with P_4 to generate novel mononuclear and dinuclear *cyclo*-P_3 complexes. The prominent characteristic features of these new *cyclo*-P_3 complexes are their unusually downfield-shifted ^{31}P NMR signals in both solution- and solid-state ^{31}P NMR spectra. DFT calculations have corroborated our experimental ^{31}P NMR results and provided an intriguing physical reason behind such anomalous ^{31}P chemical shifts. Quantum chemically, the nuclear magnetic shielding tensors can be readily calculated, and our work highlights that it is possible to understand these spectroscopic properties in a rational and intuitively comprehensible fashion. We analyzed and conceptualized the paramagnetic contribution to the nuclear magnetic shielding and the molecular response to an applied external magnetic field that gave rise to a spectral resonance that deviates dramatically from the expected values reported for other *cyclo*-P_3 complexes in the literature. Our concept puts emphasis on the small HOMO−LUMO gap as well as on the large metal contribution to the V−(*cyclo*-P_3) π-antibonding unoccupied orbital, which results in an effective mixing of frontier orbitals as well as in a dominant d(V)−p(*cyclo*-P_3) type overlap for the investigated vanadium−(*cyclo*-P_3) species in an external magnetic field. These specific couplings of orbitals manifest in significantly enhanced as well as in rerouted ligand-to-metal density currents, both inducing magnetic fields parallel to the external one and, thus, eventuating in strongly downfield-shifted phosphorus resonances. Future work will center on the delivery of *cyclo*-P_3, the isolation of a terminal vanadium phosphide, and the chemical oxidation and reduction of the *cyclo*-P_3 complexes on a preparative scale to isolate respective radical cation and anion species. As of now, we are only beginning to uncover the rich chemistry provided by these V(*cyclo*-P_3) scaffolds. The thorough understanding of their NMR spectroscopic signatures that we have established in this work will be helpful in future studies for reaction monitoring purposes.

EXPERIMENTAL DETAILS

General Considerations. Unless otherwise stated, all operations were performed in an M. Braun Lab Master double-drybox under an atmosphere of purified nitrogen or using high-vacuum standard Schlenk techniques under a nitrogen atmosphere. Anhydrous hexanes, *n*-pentane, toluene, and benzene were purchased from Aldrich in sure-sealed reservoirs (18 L) and dried by passage through two columns of activated alumina and a Q-5 column. Diethyl ether and CH_2Cl_2 were dried by passage through a column of activated alumina. THF was distilled, under nitrogen, from purple sodium benzophenone ketyl and stored under sodium metal. Distilled THF was transferred under vacuum into bombs before being pumped into a drybox. C_6D_6 was purchased from Cambridge Isotope Laboratory (CIL), degassed, and vacuum transferred to 4 Å molecular sieves. Celite, alumina, and 4 Å

DOI: 10.1021/jacs.5b10074
J. Am. Chem. Soc. 2015, 137, 15247−15261

molecular sieves were activated under vacuum overnight at 200 °C. ^{1}H, ^{13}C, ^{31}P, and ^{51}V NMR spectra were recorded on Varian 300 and 400 MHz NMR spectrometers. ^{1}H and ^{13}C NMR spectra are reported with reference to solvent resonances of C_6D_6 at 7.16 and 128.0 ppm, respectively. ^{31}P NMR chemical shifts are reported with respect to 85% H_3PO_4(aq) (0.0 ppm) standard. ^{51}V NMR chemical shifts are reported with respect to $VOCl_3$ (0.0 ppm). X-ray diffraction data were collected on a SMART6000 (Bruker) system under a stream of N_2(g) at 150 K. Elemental analysis was performed at Indiana University, Bloomington, and the University of Pennsylvania. Compounds (nacnac)VCl(Ntolyl$_2$),[19,43] (nacnac)V(Ntolyl$_2$),[19] (nacnac)VCl(OAr),[26,44] and (nacnac)V(OAr)[26] were prepared according to literature procedures. Solution magnetic studies were obtained by the method of Evans.[45]

Preparation of Fresh 0.5% Na/Hg. To a 20 mL scintillation vial was added Na chunks (104 mg, 4.52 mmol). A spatula was taken, and the Na was smeared along the side of the vial (note that the oxide surface of the Na needs to be removed before weighing it). 20.8 g of Hg was carefully added into the vial without contact with sodium. The scintillation vial was capped and tilted to allow the Na and Hg to make contact, and a puff of smoke indicated that the reaction had occurred. The vial was hot and allowed to cool to room temperature before addition of the reaction mixture. ***Caution!*** *0.5% Na/Hg is highly flammable. Disposable of sodium amalgam after reaction should be taken with precaution. The Hg waste should be confined into Hg-only waste and handled properly.*

Preparation of Fresh KC_8. The preparation of KC_8 is adapted from a literature preparation from Hegedus.[46] To a thick walled high-pressure reaction vessel is charged a glass-coated stirring bar (a black-coated stir bar can be alternatively used). The solid reactants should be well mixed and properly and securely taped prior to removal from the glovebox and placed into a preheated 150 °C oil bath. The black graphite should give way to a bronze solid. The reaction vessel should be taken back into the glovebox and again mixed to break up any remaining chunks of unmixed K. The flask is then sealed again and placed in the hot oil bath. This procedure is repeated at least three times to obtain a bronze colored laminate. Inside the glovebox, the KC_8 can be collected into a vial and stored in the freezer to extend its lifetime. ***Caution!*** *KC_8 is highly flammable. If there are remnants of KC_8, then it is best to leave it inside the glovebox exposed to the atmosphere for 2−3 days so that it can gradually become oxidized before removing it from the glovebox and quenching it with cold isopropanol.*

Purification of P_4. ***Caution!*** *P_4 is highly and immediately flammable upon exposure to air. It is also light-sensitive and should be handled with care.*

Crude P_4 is placed inside a 250 mL round-bottomed flask that is completely covered with aluminum foil so that no exposure to light is possible. Under vacuum, all water should be removed (24 h). Place the flask under vacuum on the Schlenk line with minimum exposure to light. After 24 h under vacuum, the flask is brought into the glovebox. The crude P_4 is extracted into toluene with vigorous stirring, and the solution mixture is carefully and gently heated until a homogeneous solution is obtained. The mixture is then quickly filtered through a medium porosity frit containing Celite and washed with toluene. The resulting filtrate is reduced in volume until a white solid begins to precipitate. At that point, the solution is stored in a freezer to precipitate more white solid. The solid is then filtered cold, washed with pentane, and dried under reduced pressure. *Note that all glassware and frits contaminated with P_4 should be carefully removed from the glovebox and water can be used nearby to quench any flammable P_4 residue when exposed to air. It is recommended that P_4 in this glassware be left in the box to slowly oxidize before taking it out of the glovebox.*

Purification of $CoCp^*_2$. In a 20 mL scintillation vial was dissolved 430 mg of $CoCp^*_2$ in 20 mL of hexanes, yielding a blue-green solution that was stirred for 90 min. The solution was then filtered through a medium porosity frit, and the resulting filtrate was concentrated to 5 mL. After storage at −37 °C overnight, crystalline material was isolated via filtration, washed with cold hexanes, and dried under reduced pressure.

Synthesis of (nacnac)V(*cyclo*-P_3) (OAr) (2). *Route 1: (nacnac)V(OAr) and P_4.* In a 20 mL scintillation vial at 25 °C was added (nacnac)V(OAr) (100 mg, 0.15 mmol) and 10 mL of toluene. To this solution was added solid P_4 (18.5 mg, 0.15 mmol), and the reaction mixture was allowed to stir for 2 h, leading to a yellow-brown solution. All volatiles were removed. The crude product was extracted into *n*-pentane (5 mL) and filtered through a glass pipet containing Celite. The resulting filtrate was reduced to 3 mL and stored in the freezer at −37 °C for 2 days to obtain crystalline product **2**. Yield = 63% (69.8 mg, 0.09 mmol).

Route 2: [(nacnac)V(OAr)]$_2$(μ_2-η^2:η^2-N_2) and P_4. In a 20 mL scintillation at 25 °C was added [(nacnac)V(OAr)]$_2$(μ_2-η^1:η^1-N_2) (75 mg, 0.057 mmol), P_4 (14.0 mg, 0.11 mmol), and 4 mL of toluene. The reaction mixture was transferred into a J-Young NMR tube and heated at 90 °C for 10 min. The reaction was monitored by ^{31}P NMR spectroscopy and confirmed for quantitative conversion to **2**.

Route 3: (nacnac)VCl(OAr), 0.5% Na/Hg, and P_4. At 25 °C, a 250 mL round-bottomed flask was charged with a magnetic stirring bar, and (nacnac)VCl(OAr) (580 mg, 0.85 mmol) dissolved in 25 mL of toluene was added to give a dark green solution. To this solution was added freshly prepared 0.5% Na/Hg (Na 29.3 mg, 1.27 mmol; 5.86 g Hg), and the reaction mixture was vigorously stirred for 12 h. The reaction mixture gradually transforms from dark green to brown. After the allotted time, the reaction mixture was filtered through a medium porosity frit containing Celite to remove NaCl salt residues and Hg. The brown toluene solution containing [(nacnac)V(OAr)]$_2$(μ_2-η^1:η^1-N_2) was transferred to a thick walled high-pressure reaction vessel and solid P_4 (105 mg, 0.85 mmol) was added. The reaction vessel was tightly capped, properly taped, removed from the glovebox, and placed in a preheated oil bath (90 °C) for 15 min to render a dark yellow-brown solution. The reaction vessel was allowed to cool to room temperature and returned to the glovebox, where all volatiles were removed and triturated with *n*-pentane (20 mL) and pumped off to ensure complete removal of toluene residues. The crude product was extracted into 30 mL of *n*-pentane and filtered through a medium porosity frit containing Celite to remove any unreactive P_4. Subsequent reduction of the filtrate volume (10 mL) and storage at −37 °C for 24 h produced crystalline material that was collected by decantation and dried under dynamic vacuum to give **2**. Yield = 46% (289 mg, 0.39 mmol). The *cyclo*-P_3 product was confirmed by ^{1}H and ^{31}P{^{1}H} NMR spectroscopy (C_6D_6, 25 °C). ^{1}H NMR (25 °C, 400 MHz, toluene-d_8): δ 7.41 (d, $^{3}J_{H-H}$ = 8 Hz, Ar-*H*, 1H), 7.29 (d, $^{3}J_{H-H}$ = 8 Hz, Ar-*H*, 2H), 7.07−6.95 (m, 5H, Ar-*H*), 6.89 (d, $^{3}J_{H-H}$ = 7 Hz, Ar-*H*, 1H), 6.35 (septet, 1H, C*H*(CH$_3$)$_2$), 4.77 (s, 1H, α-H), 4.42 (septet, 2H, C*H*(CH$_3$)$_2$), 2.12 (s, 6H, ArN(C*H*$_3$)CCHC(C*H*$_3$)NAr), 2.01 (br s, 3H, C*H*(CH$_3$)$_2$), 1.92 (d, $^{3}J_{H-H}$ = 6 Hz, 6H, CH(C*H*$_3$)$_2$), 1.86 (d, $^{3}J_{H-H}$ = 7 Hz, 6H, CH(C*H*$_3$)$_2$), 1.68 (br s, 6H, CH(C*H*$_3$)$_2$), 1.38 (d, $^{3}J_{H-H}$ = 6 Hz, 6H, CH(C*H*$_3$)$_2$), 0.77 (d, $^{3}J_{H-H}$ = 6 Hz, 6H, CH(C*H*$_3$)$_2$), 0.72 (d, $^{3}J_{H-H}$ = 6 Hz, 6H, CH(C*H*$_3$)$_2$). ^{13}C{^{1}H} NMR (25 °C, 400 MHz, toluene-d_8): δ 161.0 (ArN(CH$_3$)CCHC(CH$_3$)NAr), 145.0 (Ar), 141.2 (Ar), 140.6 (Ar), 139.5 (Ar), 133.3 (Ar), 122.2 (Ar), 98.6 (ArN(CH$_3$)CCHC(CH$_3$)NAr), 30.0 (CH(CH$_3$)$_2$), 27.8 (CH(CH$_3$)$_2$), 27.0 (CH(CH$_3$)$_2$), 26.4 (CH(CH$_3$)$_2$), 25.4 (CH(CH$_3$)$_2$), 25.1 (CH(CH$_3$)$_2$), 24.6 (ArN(CH$_3$)CCHC(CH$_3$)NAr)), 23.8 (CH(CH$_3$)$_2$). ^{31}P{^{1}H} NMR (25 °C, 121.5 MHz, toluene-d_8): δ 125.0 ($\Delta\nu_{1/2}$ = 324 Hz). ^{51}V NMR (25 °C, 131.5 MHz, C_6D_6): δ 2804 ($\Delta\nu_{1/2}$ = 3947 Hz). Anal. Calcd for $C_{41}H_{58}N_2OP_3V$: C, 66.66; H, 7.91; N, 3.79. Found: C, 66.75; H, 8.02; N, 3.75.

Synthesis of [(nacnac)V(Ntolyl$_2$)]$_2$(μ_2-η^2:η^3-*cyclo*-P_3) (3). In a 20 mL scintillation at 25 °C was added (nacnac)V(Ntolyl$_2$) (100 mg, 0.15 mmol) and 10 mL of toluene. To this solution was added solid P_4 (4.65 mg, 0.037 mmol), and the reaction mixture was allowed to stir for 8 h, leading to a yellow-brown solution. All volatiles were removed. The crude product was extracted into Et_2O (6 mL) and filtered through a glass pipet containing Celite. The resulting filtrate was reduced to 3 mL and stored in the freezer at −37 °C for 2 days to obtain crystalline product. Yield = 33% (35.2 mg, 0.025 mmol). ^{1}H NMR (25 °C, 400 MHz, C_6D_6): δ 14.4 ($\Delta\nu_{1/2}$ = 336 Hz), 11.4 ($\Delta\nu_{1/2}$ = 224 Hz), 9.13 ($\Delta\nu_{1/2}$ = 67.2 Hz), 8.19 ($\Delta\nu_{1/2}$ = 40 Hz), 5.39 ($\Delta\nu_{1/2}$ = 32 Hz), 3.70 ($\Delta\nu_{1/2}$ = 44 Hz), 3.30 ($\Delta\nu_{1/2}$ = 48 Hz), 1.58 ($\Delta\nu_{1/2}$ =

DOI: 10.1021/jacs.5b10074
J. Am. Chem. Soc. 2015, 137, 15247−15261

20 Hz), 1.41 ($\Delta\nu_{1/2}$ = 48 Hz), 1.01 ($\Delta\nu_{1/2}$ = 16 Hz), 0.91 ($\Delta\nu_{1/2}$ = 20 Hz), −1.82 ($\Delta\nu_{1/2}$ = 28 Hz), −10.1 ($\Delta\nu_{1/2}$ = 276 Hz). $g \approx 2$ (CW X-band EPR, 21 °C, C_6H_6); μ_{eff} = 1.80μ_B (Evans, 25 °C, C_6D_6). Anal. Calcd for $C_{86}H_{110}N_6P_3V_2$: C, 73.23; H, 7.00; N, 5.96. Found: C, 73.23; H, 8.22; N, 5.79.

Synthesis of Complex [CoCp*$_2$][1]. In a 20 mL scintillation vial was added (nacnac)V(*cyclo*-P_3) (Ntolyl$_2$) (70.0 mg, 0.092 mmol) in 5 mL of benzene. To this solution was added CoCp*$_2$ (30.0 mg, 0.091 mmol) in 5 mL of benzene and the reacton was allowed to stir for 1 h leading to the formation of a blue/green precipitate. Upon reaction completion the resulting mixture was filtered through a medium porosity frit to obtain a blue/green material which was washed with cold pentane and dried under reduced pressure. Yield =63% (63.4 mg, 0.058 mmol). ^{1}H NMR (25 °C, 400 MHz, THF-d_8) δ 7.76 ($\Delta\nu_{1/2}$ = 116 Hz), 6.55 ($\Delta\nu_{1/2}$ = 60 Hz), 1.97 ($\Delta\nu_{1/2}$ = 36 Hz) 1.42 ($\Delta\nu_{1/2}$ = 136 Hz). g_{iso} = 1.95 (CW X-band EPR, 21 °C, THF); μ_{eff} = 1.87μ_B (Evans, 25 °C, THF-d_8). Multiple attempts to obtain satisfactorily combustion analysis failed.

Solid-State ^{31}P NMR. Solid-state ^{31}P NMR spectra were obtained on a Bruker Avance 600 NMR spectrometer operating at 600.17 and 242.95 MHz for ^{1}H and ^{31}P nuclei, respectively. Powder samples were packed into zirconium oxide rotors (4 mm o.d.) in a glovebox. Spectra were recorded with direct excitation and high-power proton decoupling (70 kHz B_1 field). A recycle delay of 5 s was found to be sufficient. Typically, a few thousand transients were accumulated for each spectrum. All ^{31}P chemical shifts were referenced to 85% H_3PO_4(aq) using a solid sample of [NH_4][H_2PO_4] as a secondary external reference. Typical sample spinning frequencies for the MAS experiments are 5−14 kHz. Variable sample spinning frequencies were used to identify the isotropic peak in each spectrum.

EPR Studies. EPR spectroscopic measurements were performed in air-tight J. Young quartz tubes in an atmosphere of purified dinitrogen. Frozen solution EPR spectra were recorded on a JEOL continuous wave spectrometer JES-FA200 equipped with an X-band Gunn diode oscillator bridge, a cylindrical mode cavity, and a N_2/He cryostat. The spectra were obtained on freshly prepared solutions of the compounds and simulated using the W95EPR program written by Frank Neese (MPI for Chemical Energy Conversion, Mülheim an der Ruhr).

Cyclic Voltammetry Studies. Cyclic voltammetry was performed in 0.3 M of predried and triply recrystallized [TBA][PF_6] (*n*-tetrabutylammonium hexafluorophosphate) in anhydrous THF solution. A platinum disk (2.0 mm diameter), a platinum wire, and a silver wire were employed as the working, auxiliary, and reference electrodes, respectively. A one-compartment cell was used in the CV measurement. The electrochemical response was collected with the assistance of an E2 Epsilon (BAS) autolab potentiostat/galvanostat under the control of BAS software. All of the potentials were reported against the Fc^+/Fc couple (0.0 V). The IR drop correction was applied when significant resistance was noted. The spectrum was recorded under a N_2 atmosphere in the glovebox. In a typical experiment, 15 mg of crystalline sample (**1** or **2**) was dissolved in 5 mL of a $TBAPF_6$ solution in THF at 25 °C.

Computational Details. All geometry optimizations and frequency calculations were carried out using DFT as implemented in the Jaguar 7.0 suite of *ab initio* quantum chemistry programs.[47] Geometry optimizations were performed with B3LYP functional[34,35] and the 6-31G** basis set.[48] Vanadium and molybdenum were represented using the Los Alamos LACVP basis[49] that includes effective core potentials. The energies of the optimized structures were reevaluated by additional single-point calculations on each optimized geometry using Dunning's correlation consistent triple-ζ basis set cc-pVTZ(-f) that includes a double set of polarization functions.[36] For V and Mo, we used a modified version of LACVP, designated LACV3P, in which the exponents were decontracted to match the effective core potential with triple-ζ quality. Analytical vibrational frequencies within the harmonic approximation were computed with the 6-31G**/LACVP basis to confirm proper convergence to well-defined minima on the potential energy surface. Solvation energies were evaluated by a self-consistent reaction field[50] (SCRF) approach based on accurate numerical solutions of the Poisson−Boltzmann equation. In the results reported, solvation calculations were carried out with the 6-31G**/LACVP basis at the optimized gas-phase geometry employing the dielectric constant of ε = 7.6 for THF. As is the case for all continuum models, the solvation energies are subject to empirical parametrization of the atomic radii that are used to generate the solute surface. We employed[51] the standard set of optimized radii in Jaguar for H (1.150 Å), C (1.900 Å), N (1.600 Å), and V (1.572 Å). To compute redox potentials, the free energy in solution-phase G(sol) has been calculated as follows:

$$G(\text{sol}) = G(\text{gas}) + \Delta G^{\text{solv}} \quad (4)$$

$$G(\text{gas}) = H(\text{gas}) - TS(\text{gas}) \quad (5)$$

$$H(\text{gas}) = E(\text{SCF}) + \text{ZPE} \quad (6)$$

$$\Delta E(\text{SCF}) = \sum E(\text{SCF}) \text{ for products} - \sum E(\text{SCF}) \text{ for reactants} \quad (7)$$

$$\Delta G(\text{sol}) = \sum G(\text{sol}) \text{ for products} - \sum G(\text{sol}) \text{ for reactants} \quad (8)$$

G(gas) is the free energy in the gas phase; G(sol) is the free energy of solvation as computed using the continuum solvation model; H(gas) is the enthalpy in gas phase; T is the temperature (298.00K); S(gas) is the entropy in the gas phase; E(SCF) is the self-consistent field energy, i.e., raw electronic energy as computed from the SCF procedure; and ZPE is the zero-point energy. Note that by entropy here we refer specifically to the vibrational/rotational/translational entropy of the solute(s); the entropy of the solvent is incorporated implicitly in the continuum solvation model. Computed redox potentials have been referenced to Fc/Fc^+ with computed absolute reduction potential of 5.211 V in THF.

^{31}P chemical shift (CS) and tensor calculations were performed using Amsterdam Density Functional[52] (ADF2009.1) using the built-in EPR module.[53] The BP86 functional[54,34b] in combination with the all-electron TZ2P basis set was used in all ADF calculations. Relativistic effects were taken into account using Pauli-type Hamiltonian,[55] whereas the gauge-including atomic orbital (GIAO) approach[56] was employed to compute ^{31}P shielding parameters. Similar to the experimental protocol, computed ^{31}P chemical shifts are calibrated such that H_3PO_4 is 0.0 ppm, where the computed σ (H_3PO_4) is 301.3 ppm. It is important to note that to compute pairwise orbital contributions to the shielding tensor with the EPR module the molecular structure has to be defined in the PAS of the selected atom, which also has to be set as the origin of the coordinate system.

■ ASSOCIATED CONTENT

Supporting Information

The Supporting Information is available free of charge on the ACS Publications website at DOI: 10.1021/jacs.5b10074.

Crystallographic data and tables, NMR spectra, and computational details (PDF)
Crystallographic data (CIF, CIF, CIF)

■ AUTHOR INFORMATION

Corresponding Authors

*(M.-H.B.) mbaik2805@kaist.ac.kr
*(D.J.M.) mindiola@sas.upenn.edu

Notes

The authors declare no competing financial interest.

■ ACKNOWLEDGMENTS

This work was supported by the Chemical Sciences, Geosciences, and Biosciences Division, Office of Basic Energy Sciences, Office of Science, U.S. Department of Energy (DE-

DOI: 10.1021/jacs.5b10074
J. Am. Chem. Soc. 2015, 137, 15247−15261

FG02-07ER15893, awarded to D.J.M.). Rick Thompson is thanked for obtaining single crystals of complex **3**. B.P. thanks the Research Foundation Flanders, FWO (1279414N) for financial support. K.M. and E.M.Z. thank the Friedrich-Alexander University Erlangen-Nürnberg (FAU) and, also B.P., the COST Action CM1305 ECOSTBio (Explicit Control over Spin-States in Technology and Biochemistry) for financial support of this work. G.W. thanks the NSERC of Canada for financial support. S.F. thanks the NSF for an American Competitiveness in Chemistry Fellowship (CHE-1137284).

REFERENCES

(1) For a recent review, see Cossairt, B. M.; Piro, N. A.; Cummins, C. C. *Chem. Rev.* **2010**, *110*, 4164.
(2) Lynam, J. M. *Angew. Chem., Int. Ed.* **2008**, *47*, 831.
(3) Stephens, F. H.; Johnson, M. J. A.; Cummins, C. C.; Kryatova, O. P.; Kryatov, S. V.; Rybak-Akimova, E. V.; McDonough, J. E.; Hoff, C. D. *J. Am. Chem. Soc.* **2005**, *127*, 15191.
(4) Piro, N. A.; Cummins, C. C. *J. Am. Chem. Soc.* **2008**, *130*, 9524.
(5) Tofan, D.; Cossairt, B. M.; Cummins, C. C. *Inorg. Chem.* **2011**, *50*, 12349.
(6) Cossairt, B. M.; Cummins, C. C. *J. Am. Chem. Soc.* **2009**, *131*, 15501.
(7) Di Vaira, M.; Ghilardi, C. A.; Midollini, S.; Sacconi, L. *J. Am. Chem. Soc.* **1978**, *100*, 2550.
(8) Ehses, M.; Romerosa, A.; Peruzzini, M. In *New Aspects in Phosphorus Chemistry I*; Majoral, J.-P., Ed.; Springer: Berlin, 2002.
(9) Di Vaira, M.; Stoppioni, P.; Peruzzini, M. *Polyhedron* **1987**, *6*, 351.
(10) Di Vaira, M.; Sacconi, L. *Angew. Chem., Int. Ed. Engl.* **1982**, *21*, 330.
(11) Scherer, O. J.; Werner, B.; Heckmann, G.; Wolmershäuser, G. *Angew. Chem., Int. Ed. Engl.* **1991**, *30*, 553.
(12) (a) Scherer, O. J. *Acc. Chem. Res.* **1999**, *32*, 751. (b) Whitmire, K. H. *Adv. Organomet. Chem.* **1998**, *42*, 1. (c) Scherer, O. J. *Angew. Chem., Int. Ed. Engl.* **1990**, *29*, 1104. For some other reviews of *cyclo*-P_3 and metal-phosphorus complexes, see (d) Caporali, M.; Gonsalvi, L.; Rossin, A.; Peruzzini, M. *Chem. Rev.* **2010**, *110*, 4178.
(13) Bianchini, C.; Di Vaira, M.; Meli, A.; Sacconi, L. *Angew. Chem., Int. Ed. Engl.* **1980**, *19*, 405.
(14) Bianchini, C.; Di Vaira, M.; Meli, A.; Sacconi, L. *Inorg. Chem.* **1981**, *20*, 1169.
(15) Bianchini, C.; Di Vaira, M.; Meli, A.; Sacconi, L. *J. Am. Chem. Soc.* **1981**, *103*, 1448.
(16) Cecconi, F.; Dapporto, P.; Midollini, S.; Sacconi, L. *Inorg. Chem.* **1978**, *17*, 3292.
(17) Dapporto, P.; Sacconi, L.; Stoppioni, P.; Zanobini, F. *Inorg. Chem.* **1981**, *20*, 3834.
(18) Cossairt, B. M.; Diawara, M.-C.; Cummins, C. C. *Science* **2009**, *323*, 602.
(19) Tran, B. L.; Singhal, M.; Park, H.; Lam, O. P.; Pink, M.; Krzystek, J.; Ozarowski, A.; Telser, J.; Meyer, K.; Mindiola, D. J. *Angew. Chem., Int. Ed.* **2010**, *49*, 9871.
(20) Chisholm, M. H.; Huffman, J. C.; Pasterczyk, J. W. *Inorg. Chim. Acta* **1987**, *133*, 17.
(21) Goh, L. Y.; Chu, C. K.; Wong, R. C. S.; Hambley, T. W. *J. Chem. Soc., Dalton Trans.* **1989**, 1951.
(22) (a) Scherer, O. J.; Sitzmann, H.; Wolmershaüser, G. *J. Organomet. Chem.* **1984**, *268*, C9. (b) Umbarkar, S.; Sekar, P.; Scheer, M. *Dalton Trans.* **2000**, 1135.
(23) Cossairt, B. M.; Cummins, C. C.; Head, A. R.; Lichtenberger, D. L.; Berger, R. J. F.; Hayes, S. A.; Mitzel, N. W.; Wu, G. *J. Am. Chem. Soc.* **2010**, *132*, 8459.
(24) Fabbrizzi, L.; Sacconi, L. *Inorg. Chim. Acta* **1979**, *36*, L407–L408.
(25) Clark, J. R.; Pulvirenti, A. L.; Fanwick, P. E.; Sigalas, M.; Eisenstein, O.; Rothwell, I. P. *Inorg. Chem.* **1997**, *36*, 3623.
(26) Tran, B. L.; Pinter, B.; Nichols, A. J.; Chen, C.-H.; Konopka, F. T.; Thompson, R.; Krzystek, J.; Ozarowski, A.; Telser, J.; Baik, M.-H.; Meyer, K.; Mindiola, D. J. *J. Am. Chem. Soc.* **2012**, *134*, 13035.
(27) (a) Robin, M. D.; Day, P. *Adv. Inorg. Chem.* **1967**, *10*, 247. For an example of a Class II system involving a dinuclear V(III)/V(IV) system, see (b) Rambo, J. R.; Castro, S. L.; Folting, K.; Bartley, S. L.; Heintz, R. A.; Christou, G. *Inorg. Chem.* **1996**, *35*, 6844.
(28) (a) Thomas, C. D.; Gingrich, N. S. *J. Chem. Phys.* **1938**, *6*, 659. (b) Gingrich, N. S. *Rev. Mod. Phys.* **1943**, *15*, 90. (c) Simon, A.; Borrmann, H.; Horakh, J. J. *Chem. Ber.* **1997**, *130*, 1235.
(29) Di Vaira, M.; Stoppioni, P. *Polyhedron* **1994**, *13*, 3045–3051.
(30) Di Vaira, M.; Stoppioni, P.; Peruzzini, M. *J. Chem. Soc., Dalton Trans.* **1990**, 109–113.
(31) Evans, D. H.; O'Connell, K. M.; Petersen, R. A.; Kelly, M. J. *J. Chem. Educ.* **1983**, *60*, 290.
(32) Kissinger, P. T.; Heineman, W. R. *J. Chem. Educ.* **1983**, *60*, 702.
(33) Runo, J. R.; Peters, D. G. *J. Chem. Educ.* **1993**, *70*, 708.
(34) (a) Becke, A. D. *J. Chem. Phys.* **1993**, *98*, 5648. (b) Becke, A. D. *Phys. Rev. A: At., Mol., Opt. Phys.* **1988**, *38*, 3098.
(35) Lee, C. T.; Yang, W. T.; Parr, R. G. *Phys. Rev. B: Condens. Matter Mater. Phys.* **1988**, *37*, 785.
(36) (a) Dunning, T. H. *J. Chem. Phys.* **1989**, *90*, 1007.
(37) Albright, T. A.; Burdett, J. K.; Whangbo, M. H. *Orbital Interactions in Chemistry*; Wiley: New York, 1985.
(38) Connelly, N. G.; Geiger, W. E. *Chem. Rev.* **1996**, *96*, 877.
(39) (a) Widdifield, M.; Schurko, R. W. *Concepts Magn. Reson., Part A* **2009**, *34A*, 91. (b) Schreckenbach, G.; Wolff, S. K.; Ziegler, T. *J. Phys. Chem. A* **2000**, *104*, 8244. (c) Wu, G.; Rovnyak, D.; Johnson, M. J. A.; Zanetti, N. C.; Musaev, D. G.; Morokuma, K.; Schrock, R. R.; Griffin, R. G.; Cummins, C. C. *J. Am. Chem. Soc.* **1996**, *118*, 10654. (d) Wu, G.; Zhu, J.; Mo, X.; Wang, R.; Terskikh, V. *J. Am. Chem. Soc.* **2010**, *132*, 5143.
(40) Ramsey, N. F. *Phys. Rev.* **1950**, *78*, 699. (b) Pople, J. A. *Proc. R. Soc. London, Ser. A* **1957**, *239*, 541. (c) Pople, J. A. *Discuss. Faraday Soc.* **1962**, *34*, 7.
(41) For a simpler conceptual understanding, we formally identified ground and excited electronic states with occupied and unoccupied orbitals, respectively, as shown in eq 3 and corresponding discussions. For further details, see ref 39a.
(42) (a) Zhu, J.; Kurahashi, T.; Fujii, H.; Wu, G. *Chem. Sci.* **2012**, *3*, 391. (b) Zhu, J.; Lau, J. Y. C.; Wu, G. *J. Phys. Chem. B* **2010**, *114*, 11681.
(43) Tran, B. L.; Pink, M.; Gao, X.; Park, H.; Mindiola, D. J. *J. Am. Chem. Soc.* **2010**, *132*, 1458.
(44) Tran, B. L.; Krzystek, J.; Ozarowski, A.; Chen, C.-H.; Pink, M.; Karty, J. A.; Telser, J.; Meyer, K.; Mindiola, D. J. *Eur. J. Inorg. Chem.* **2013**, *2013*, 3916.
(45) (a) Pass, G.; Sutcliffe, H. *Practical Inorganic Chemistry*; Chapman and Hall: London, 1968. (b) Teweldemedhin, Z. S.; Fuller, R. L.; Greenblatt, M. *J. Chem. Educ.* **1996**, *73*, 906. (c) Cai, S.; Walker, F. A.; Licoccia, S. *Inorg. Chem.* **2000**, *39*, 3466.
(46) Schwindt, M. A.; Lejon, T.; Hegedus, L. S. *Organometallics* **1990**, *9*, 2814.
(47) *Jaguar 7.0*; Schrödinger, LLC: New York, 2007.
(48) (a) Ditchfield, R.; Hehre, W. J.; Pople, J. A. *J. Chem. Phys.* **1971**, *54*, 724. (b) Hariharan, P. C.; Pople, J. A. *Theor. Chem. Acc.* **1973**, *28*, 213.
(49) (a) Wadt, W. R.; Hay, P. *J. Chem. Phys.* **1985**, *82*, 284. (b) Hay, P. J.; Wadt, W. R. *J. Chem. Phys.* **1985**, *82*, 270.
(50) (a) Marten, B.; Kim, K.; Cortis, C.; Friesner, R. A.; Murphy, R. B.; Ringnalda, M. N.; Sitkoff, D.; Honig, B. *J. Phys. Chem.* **1996**, *100*, 11775. (b) Friedrichs, M.; Zhou, R. H.; Edinger, S. R.; Friesner, R. A. *J. Phys. Chem. B* **1999**, *103*, 3057. (c) Edinger, S. R.; Cortis, C.; Shenkin, P. S.; Friesner, R. A. *J. Phys. Chem. B* **1997**, *101*, 1190.
(51) Rashin, A. A.; Honig, B. *J. Phys. Chem.* **1985**, *89*, 5588.
(52) (a) te Velde, G.; Bickelhaupt, F. M.; Baerends, E. J.; Fonseca Guerra, C.; van Gisbergen, S. J. A.; Snijders, J. G.; Ziegler, T. *J. Comput. Chem.* **2001**, *22*, 931. (b) Fonseca Guerra, C.; Snijders, J. G.; te Velde, G.; Baerends, E. J. *Theor. Chem. Acc.* **1998**, *99*, 391.

DOI: 10.1021/jacs.5b10074
J. Am. Chem. Soc. 2015, 137, 15247–15261

(c) Baerends, E. J.; Autschbach, J.; Bashford, D.; Børces, A.; Bickelhaupt, F. M.; Bo, C.; Boerrigter, P. M.; Cavallo, L.; Chong, D. P.; Deng, L.; Dickson, R. M.; Ellis, D. E.; van Faassen, M.; Fan, M.; Fischer, T. H.; Fonseca Guerra, C.; Ghysels, A.; Giammona, A.; van Gisbergen, S. J. A.; Gçtz, A. W.; Groeneveld, J. A.; Gritsenko, O. V.; Grüning, M.; Harris, F. E.; Harris, P.; van den Hoek, P.; Jacob, C. R.; Jacobsen, H.; Jensen, L.; van Kessel, G.; Kootstra, F.; Krykunov, M. V.; van Lenthe, E.; McCormack, D. A.; Michalak, A.; Mitoraj, M.; Neugebauer, J.; Nicu, V. P.; Noodleman, L.; Osinga, V. P. O.; Patchkovskii, S.; Philipsen, P. H. T.; Post, D.; Pye, C. C.; Ravenek, W.; Rodriguez, J. I.; Ros, P.; Schipper, P. R. T.; Schreckenbach, G.; Seth, M.; Snijders, J. G.; Solà, M.; Swart, M.; Swerhone, D.; te Velde, G.; Vernooijs, P.; Versluis, L.; Visscher, L.; Visser, O.; Wang, F.; Wesolowski, T. A.; van Wezenbeek, E. M.; Wiesenekker, G.; Wolff, S. K.; Woo, T. K.; Yakovlev, A. L.; Ziegler, T. *ADF2009.01*; Scientific Computing & Modeling: Amsterdam, The Netherlands. http://www.scm.com.

(53) Schreckenbach, G.; Ziegler, T. *J. Phys. Chem. A* **1997**, *101*, 3388.

(54) Perdew, J. P. *Phys. Rev. B: Condens. Matter Mater. Phys.* **1986**, *33*, 8822.

(55) (a) Snijders, J. G.; Baerends, E. J. *Mol. Phys.* **1978**, *36*, 1789. (b) Snijders, J. G.; Baerends, E. J.; Ros, P. *Mol. Phys.* **1979**, *38*, 1909. (c) Ziegler, T.; Snijders, J. G.; Baerends, E. J. *J. Chem. Phys.* **1981**, *74*, 1271.

(56) (a) Schreckenbach, G.; Ziegler, T. J. *J. Phys. Chem.* **1995**, *99*, 606. (b) Schreckenbach, G.; Ziegler, T. *Int. J. Quantum Chem.* **1997**, *61*, 899.

DOI: 10.1021/jacs.5b10074
J. Am. Chem. Soc. 2015, 137, 15247−15261